

ARTICLE

Uncovering the dosage-dependent roles of *Arid1a* in gastric tumorigenesis for combinatorial drug therapy

Adrian Kwan Ho Loe^{1,2*}, Roshane Francis^{1,2*}, Jieun Seo^{1,2,3}, Lutao Du^{4,5}, Yunshan Wang^{4,5}, Ji-Eun Kim^{1,2}, Shaheed W. Hakim⁶, Jung-Eun Kim^{1,2}, Housheng Hansen He^{7,8}, Haiyang Guo^{4,5,7}, and Tae-Hee Kim^{1,2}

Gastric cancer (GC) is one of the most common deadly cancers in the world. Although patient genomic data have identified *AT-rich interaction domain 1A (ARID1A)*, a key chromatin remodeling complex subunit, as the second most frequently mutated gene after *TP53*, its *in vivo* role and relationship to *TP53* in gastric tumorigenesis remains unclear. Establishing a novel mouse model that reflects the *ARID1A* heterozygous mutations found in the majority of human GC cases, we demonstrated that *Arid1a* heterozygosity facilitates tumor progression through a global loss of enhancers and subsequent suppression of the p53 and apoptosis pathways. Moreover, mouse genetic and single-cell analyses demonstrated that the homozygous deletion of *Arid1a* confers a competitive disadvantage through the activation of the p53 pathway, highlighting its distinct dosage-dependent roles. Using this unique vulnerability of *Arid1a* mutated GC cells, our combined treatment with the epigenetic inhibitor, TP064, and the p53 agonist, Nutlin-3, inhibited growth of *Arid1a* heterozygous tumor organoids, providing a novel therapeutic option for GC.

Introduction

As the third deadliest cancer worldwide, gastric cancer (GC) accounted for an estimated 8% of all cancer mortality in 2019 (Ferlay et al., 2019). One striking feature of the GC genome is a high incidence of mutations altering chromatin modifiers. Indeed, mutations in genes for BRG1- or HBRM-associated factors (BAF) chromatin remodeling complex proteins (*ARID1A* mutations at 14–31%, *ARID1B* at 9%) and nucleosome remodeling deacetylase complex proteins (*CHD3* at 8%, *CHD4* at 9%) are collectively very common (The Cancer Genome Atlas Research Network, 2014; Cerami et al., 2012; Gao et al., 2013; Wang et al., 2011). Histone methyltransferase genes also are frequently mutated (*MLL1-MLL4* at 9–21%; The Cancer Genome Atlas Research Network, 2014; Cerami et al., 2012; Gao et al., 2013; Zang et al., 2012). These types of mutations suggest a prominent role for altered chromatin organization in gastric tumorigenesis, but the *in vivo* roles of these chromatin modifiers have been poorly understood due to the limitation of relevant GC animal models. Moreover, the mutations in these chromatin modifier genes also overlap with other GC mutations such as *TP53*, the most mutated GC gene. However, it remains unclear how altered chromatin modifiers cooperate with the p53 pathway to promote gastric tumorigenesis.

The BAF complex is an ATP-dependent chromatin remodeling complex that mobilizes nucleosomes and regulates global histone modification (Kadoch and Crabtree, 2015). The BAF complex is the most commonly mutated chromatin modifier in human malignancies, and many subunits of the complex have been linked to a wide spectrum of cancers (Kadoch and Crabtree, 2015). Notably, *AT-rich interaction domain 1A (ARID1A)*, a subunit of the BAF complex, has been identified as the second most mutated gene after *TP53* in GC (The Cancer Genome Atlas Research Network, 2014). Consistent with *ARID1A* mutations found in various types of cancer, it has been known primarily to have tumor suppressor roles in other tissues (Wu and Roberts, 2013). Several studies showed that its tissue-specific deletion promotes pancreatic and intestinal tumorigenesis *in vivo* (Kimura et al., 2018; Mathur et al., 2017; Wang et al., 2019). Interestingly, liver-specific deletion of *Arid1a* at early stages conferred resistance to tumor initiation, whereas its deletion in established tumors facilitated tumor progression, indicating its tissue-specific roles (Sun et al., 2017). In GC, recent clinical studies have shown that *ARID1A* deficiency is associated with poor prognosis and lymph node metastasis (Aso et al., 2015; Han

¹Program in Developmental & Stem Cell Biology, The Hospital for Sick Children, Toronto, Ontario, Canada; ²Department of Molecular Genetics, University of Toronto, Toronto, Ontario, Canada; ³Department of Biomedical Sciences, Seoul National University College of Medicine, Seoul, Korea; ⁴Department of Clinical Laboratory, The Second Hospital of Shandong University, Jinan, Shandong, China; ⁵Tumor Marker Detection Engineering Laboratory of Shandong Province, Jinan, Shandong, China; ⁶St. Joseph's Health Centre, Unity Health Toronto, Toronto, Ontario, Canada; ⁷Princess Margaret Cancer Centre, University Health Network, Toronto, Ontario, Canada; ⁸Department of Medical Biophysics, University of Toronto, Toronto, Ontario, Canada.

*A.K.H. Loe and R. Francis contributed equally to this paper; Correspondence to Tae-Hee Kim: tae-hee.kim@sickkids.ca; Haiyang Guo: haiyang.guo@email.sdu.edu.cn.

© 2021 Loe et al. This article is distributed under the terms of an Attribution–Noncommercial–Share Alike–No Mirror Sites license for the first six months after the publication date (see <http://www.rupress.org/terms/>). After six months it is available under a Creative Commons License (Attribution–Noncommercial–Share Alike 4.0 International license, as described at <https://creativecommons.org/licenses/by-nc-sa/4.0/>).

et al., 2016; Inada et al., 2015; Yang et al., 2016). Several cell culture studies have provided some evidence supporting its role as a tumor suppressor in GC. Knockdown of *ARID1A* in GC cell lines promoted proliferation, migration, and survival (Nag et al., 2005; Yan et al., 2014; Yang et al., 2018). However, its *in vivo* role remains unclear.

To define the mechanistic role of *Arid1a* in gastric tumorigenesis, we generated a clinically relevant gastric tumor model with an *Arid1a* heterozygous deletion. We found that *Arid1a* heterozygous tumors exhibit a global loss of active enhancer marks and down-regulation of the p53 and apoptotic pathway genes, leading to enhanced tumor growth and progression. Surprisingly, during GC development, homozygous deletion of *Arid1a* in gastric tumors conferred a competitive disadvantage through abnormal activation of the p53 pathway. Using this vulnerability of *Arid1a* mutated tumor cells, we were able to design a combinatorial treatment consisting of an epigenetic inhibitor and a p53 agonist that synergistically inhibits the growth of organoids established from *Arid1a* heterozygous tumors. This novel approach provides a potentially effective therapeutic option for GC patients harboring *ARID1A* mutations.

Results

Arid1a heterozygosity promotes tumor progression *in vivo*

To examine the correlation between tumor progression and *ARID1A* expression in GC, we analyzed human GC samples by performing histology. This analysis categorized them into four different groups: benign, well, moderately, and poorly differentiated groups (Fig. 1 A). *ARID1A* staining showed its significantly reduced expression in moderately differentiated gastric tumors compared with the benign tissue (Fig. 1 B). While poorly differentiated gastric tumors exhibit higher levels of *ARID1A* expression than moderately differentiated gastric tumors, they display a lower level of its expression than the benign tissue (Fig. 1 B). In matched tumor-normal pair analyses, we found that gastric tumors consistently exhibit a lower level of *ARID1A* expression than the benign tissue in all pairs, further supporting that *ARID1A* loss may be a driver for gastric tumorigenesis (Fig. 1 C).

To further examine the dynamics of *ARID1A* expression observed in GC, we defined the different types of *ARID1A* mutations in human GC patients by analyzing genomic data collected by The Cancer Genome Atlas (TCGA) Research Network. Interestingly, we observed that most *ARID1A* alterations found in GC patients were shallow deletions or single-copy truncations, suggesting haploinsufficiency of *ARID1A* in GC (Fig. 1 D; Cerami et al., 2012; Gao et al., 2013). Furthermore, we found that *ARID1A* heterozygosity is correlated with more advanced stages of GC (Fig. S1 A). To address, for the first time, the *in vivo* role of *Arid1a* heterozygosity during gastric tumor progression, we generated a clinically relevant gastric tumor model by combining *Arid1a* heterozygosity and the pro-proliferative signaling pathway, Notch signaling.

Notch signaling is frequently activated in GC (Yao et al., 2017), and its ectopic activation in gastric parietal cells (*Atp4b*^{Cre}; *Rosa26*^{NICD}) induces their dedifferentiation to stem cells and leads

to adenoma formation in the gastric corpus region (Fig. 1 E; Kim and Shivdasani, 2011). Notably, copy number variation and gene expression analyses showed that amplification of Notch pathway genes significantly co-occurs with *ARID1A* heterozygosity in human GC (Fig. 1 F and Fig. S1 B) and that significantly higher expression of Notch pathway genes is found in *ARID1A* heterozygous GC than in wild-type GC (Fig. S1 C). Given the clinical relevance of activated Notch signaling co-occurring with *ARID1A* heterozygosity in human GC, we used this model to specifically target *Arid1a* in the gastric corpus region.

After confirming *ARID1A* expression in the stomach of *Atp4b*^{Cre};*Rosa26*^{NICD} mice (Fig. S1 D), we deleted one copy of *Arid1a* in this model (*Atp4b*^{Cre};*Rosa26*^{NICD};*Arid1a*^{lox/+}; Fig. S1 E). Compared with the *Arid1a* intact controls, mice with a single copy of *Arid1a* developed larger tumors (Fig. 1 G), and further histological analyses revealed enhanced glandular hyperplasia at 10 wk (Fig. 1, H and I). In addition, staining for the proliferation marker, Ki67, identified an increased number of proliferating cells in *Arid1a* heterozygous adenomas compared with *Arid1a* intact adenomas, suggesting that the enhanced tumor growth may be due in part to increased proliferation (Fig. 1, J and K).

To further characterize the effect of *Arid1a* loss in our gastric tumor model, we analyzed the tumors using additional features indicative of tumor progression (Table S1). In a comparison with *Arid1a* intact adenomas, we found enhanced intestinal metaplasia at 10 wk and a significant increase in inflammation and foveolar hyperplasia at 25 wk in *Arid1a* heterozygous adenomas (Fig. 1 L; and Fig. S1, F and G). By combining these disease features, we calculated a cumulative disease score and found a significantly increased score in *Arid1a* heterozygous adenoma mice compared with *Arid1a* intact adenoma mice (Fig. 1 M). Additional scoring of tumors at 25 wk showed a significant increase in the number of tumors with high-grade dysplasia for *Arid1a* heterozygous adenoma mice compared with the *Arid1a* intact adenoma mice (Fig. 1 N). Together, this work demonstrates, for the first time, a tumor-suppressive *in vivo* role for *Arid1a* in gastric tumor progression.

Global loss of active enhancer marks and down-regulation of the p53 and apoptosis pathway genes by *Arid1a* heterozygosity

To define the chromatin changes induced by *Arid1a* heterozygosity in our adenoma model, we performed chromatin immunoprecipitation sequencing (ChIP-seq) with gastric epithelial cells isolated from both *Arid1a* intact and heterozygous adenoma mice, as well as from normal (*Cre*⁻ control) mice. We then analyzed histone modifications for active cis-regulatory elements (i.e., H3K27ac, H3K4me3) typically regulated by the BAF complex (Fig. 2 A). We observed an overall increase in the number of H3K27ac and H3K4me3 peaks in the *Arid1a* intact tumors compared with the normal stomachs (Fig. 2 B and Fig. S2 A). However, the loss of one copy of *Arid1a* led to a dramatic reduction in the number of peaks across the genome (Fig. 2 B and Fig. S2 A). Since H3K27ac marks both active promoter and enhancer regions, we categorized the peaks into either enhancers or promoters based on proximity to the transcriptional start site (Fig. S2 B). Strikingly, we found that a majority of both promoter and enhancer peaks were lost in *Arid1a* heterozygous tumors

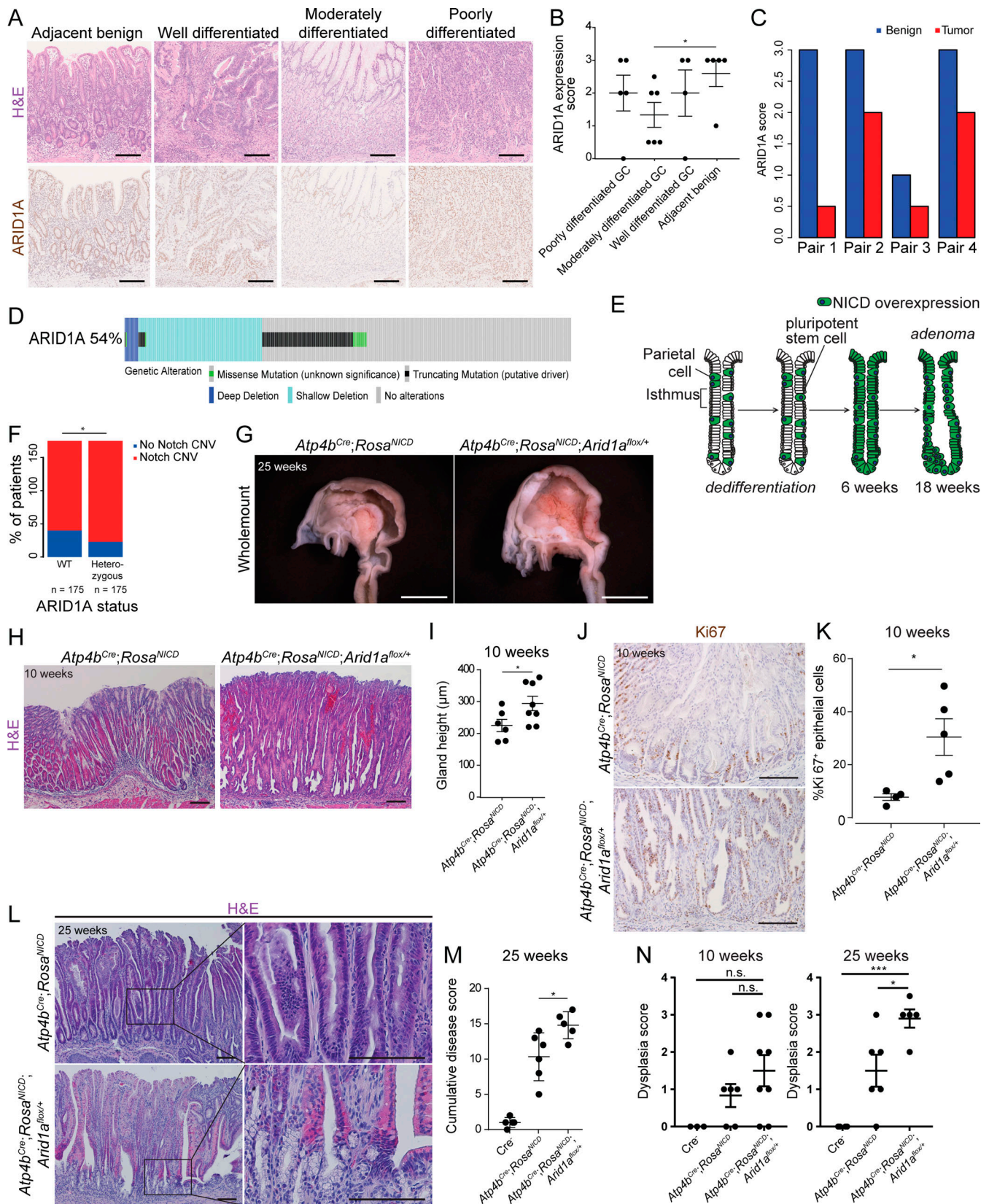


Figure 1. **Promotion of gastric tumor progression by *Arid1a* heterozygosity.** (A) Histological images and ARID1A staining of human GC samples with different tumor grades. Scale bars, 100 μm. (B) Quantification of ARID1A protein level using ARID1A staining of human GC samples with different tumor grades (*, P = 0.048). Bars represent mean ± SEM. (C) Quantification of ARID1A protein level from ARID1A staining between tumor and adjacent benign tissues in the same tumor-normal pairs. (D) Summary of *ARID1A* alterations found in human GC patients using DNA-sequencing data obtained from TCGA (STAD, Firehose)

and visualized using cBioportal OncoPrint (Cerami et al., 2012; Gao et al., 2013). Among the 54% of all GC samples that exhibit *ARID1A* mutations, the majority of *ARID1A* alterations (87%) are functionally heterozygous, occurring either as a single truncation mutation (in black) or as a shallow deletion (in light blue). **(E)** Diagram outlining adenoma formation in the Notch-driven gastric adenoma model. NICD, Notch1 intracellular domain. **(F)** Analysis of TCGA-STAD data showing the proportion of *ARID1A* wild-type or *ARID1A* heterozygous GC samples that contain amplification for genes related to Notch signaling (*, $P = 0.026$, χ^2 test). **(G)** Whole-mount images of the gastric lumen comparing *Arid1a* heterozygous adenoma mice with adenoma mice with intact *Arid1a*, showing larger tumors in the former ($n = 5$ each). Scale bars, 5 mm. **(H)** Representative histological images of *Arid1a* intact and *Arid1a* heterozygous gastric adenoma at an early stage of tumor progression ($n = 6-8$ each). Scale bars, 100 μm . Bars represent mean \pm SEM. **(I)** Quantification of gastric gland height confirms a significant increase in gland height of *Arid1a* heterozygous tumors compared with *Arid1a* intact tumors at initial stages of tumor progression (*, $P = 0.045$, unpaired t test). **(J)** Representative images of Ki67 staining, a marker of proliferating cells, in *Arid1a* intact and *Arid1a* heterozygous tumors at 10 wk ($n = 4-5$ each). Scale bars, 100 μm . **(K)** Quantification of Ki67⁺ cells in the epithelium of *Arid1a* intact and *Arid1a* heterozygous tumors at 10 wk (*, $P = 0.024$, unpaired t test). Bars represent mean \pm SEM. **(L)** Representative histological images of *Arid1a* intact and *Arid1a* heterozygous gastric adenoma at late stage (25 wk) of tumor progression ($n = 5-6$ each). Scale bars, 100 μm . **(M)** Histopathological scoring of late-stage tumors shows a significant increase in the cumulative disease score of *Arid1a* heterozygous tumors compared with *Arid1a* intact tumors using features shown in Table S1 (*, $P = 0.028$, unpaired t test). Bars represent mean \pm SEM. **(N)** Histopathological scoring of dysplasia using features shown in Table S1 indicates no significant difference between *Arid1a* intact and heterozygous tumors at an early stage. At late stages, *Arid1a* heterozygous tumors have a significantly higher dysplastic index than *Arid1a* intact tumors (*, $P < 0.05$; ***, $P < 0.001$; unpaired t test). Bars represent mean \pm SEM.

compared with *Arid1a* intact tumors; 11,067 promoter and 7,354 enhancer regions were unique to *Arid1a* intact tumors (Fig. 2 C and Table S2). While pathway enrichment analysis did not identify any pathways unique to promoter peaks in *Arid1a* intact tumors (Fig. S2 C), we found an enrichment for enhancer peaks related to apoptosis genes, such as *Casp8* and *Fos*, in the *Arid1a* intact tumors but not the *Arid1a* heterozygous tumors (Fig. 2, D and E). Transcription factor motif analysis identified enrichment of Notch effectors, HES1 and HES7, in common (*Arid1a* intact and heterozygous) enhancer peaks, supporting *Arid1a*- and Notch signaling-mediated gastric tumor progression (Fig. S2 D).

To determine if the changed H3K27ac landscape due to *Arid1a* heterozygosity influences downstream gene expression, we also performed RNA sequencing (RNA-seq) under the same conditions (Fig. 2 A). Of the genes that have lost promoter and enhancer H3K27ac marks in *Arid1a* heterozygous tumors compared with *Arid1a* intact tumors, 208 and 171 genes, respectively, were down-regulated (Fig. 2 F). We also found that *Arid1a* heterozygous tumors have an expression profile more similar to that of normal stomachs than *Arid1a* intact tumors (Fig. 2 G). We then further categorized the dysregulated genes into four groups: (A) genes that are up-regulated in both *Arid1a* intact and *Arid1a* heterozygous tumors compared with normal stomachs, (B) genes that are down-regulated in both *Arid1a* intact and *Arid1a* heterozygous tumors compared with normal stomachs, (C) genes that are up-regulated in *Arid1a* intact tumors but not in *Arid1a* heterozygous tumors when compared with normal stomachs, and (D) genes that are down-regulated in *Arid1a* intact tumors but not in *Arid1a* heterozygous tumors when compared with normal stomachs (Fig. 2 G and Table S3). Group C and D contained genes that are dysregulated between the *Arid1a* intact tumors and *Arid1a* heterozygous tumors. To study the function of these genes, we performed pathway enrichment analysis for groups B, C, and D and found apoptosis and p53 signaling to be enriched in group C, while processes related to fatty acid metabolism were enriched in group D (Fig. 2, H and I). To validate our findings, we performed quantitative RT-PCR (RT-qPCR) using gastric epithelial cells isolated from *Arid1a* intact and *Arid1a* heterozygous tumors. We found that expression levels of *Arid1a* as well as p53 pathway and apoptosis genes, such as *Fos*,

Bax, and *Casp8*, are significantly down-regulated in *Arid1a* heterozygous tumors compared with *Arid1a* intact tumors (Fig. 2 J and Fig. S2 E). To quantitatively analyze apoptosis using flow cytometry, we isolated epithelial cells (epithelial cell adhesion molecule positive [Epcam⁺]) from tumors and stained them with annexin V and propidium iodide (PI). While there was no difference in the proportion of cells undergoing early apoptosis (annexin V⁺ PI⁻), we found a significant reduction of late apoptotic cells (annexin V⁺ PI⁺) in *Arid1a* heterozygous tumors compared with *Arid1a* intact tumors (Fig. S2, F and G). Although a downward trend was observed, cleaved caspase-3 antibody staining did not show a significant reduction of apoptotic cells in *Arid1a* heterozygous tumors compared with *Arid1a* intact tumors (Fig. S2, H and I). These data suggest that the loss of one copy of *Arid1a* results in a moderate suppression of apoptosis, leading to the increased tumor growth observed in gastric tumors at later stages (25 wk). We were also unable to identify a significant difference in expression of p53 proteins between *Arid1a* intact or *Arid1a* heterozygous tumors, suggesting that the activation of p53 signaling and apoptosis observed in our tumor model may be caused by activation of enhancers and genes downstream of p53 rather than the accumulation of p53 protein itself (Fig. S2, J and K).

To determine whether the enhancers activated in *Arid1a* intact tumors were also associated with the p53 and apoptosis pathway genes, we calculated the overlap between the H3K27ac peaks in *Arid1a* intact tumors and potential enhancer regions (± 50 kb to approximately ± 2 kb from transcription start sites) of the p53 and apoptosis pathway genes. We then compared it with the genome background (the overlap between those H3K27ac peaks enhancer regions of random genes). Indeed, we observed a significant increase in the overlap between the H3K27ac peaks in the *Arid1a* intact tumors and apoptosis/p53 pathway enhancer regions compared with the background. However, this overlap was markedly reduced in *Arid1a* heterozygous tumors, suggesting *Arid1a* heterozygosity-mediated regulation of apoptosis/p53 pathway enhancers (Fig. 2 K). Together, these experiments showed that heterozygous deletion of *Arid1a* in gastric tumors leads to a global loss of H3K27ac marked enhancers and the subsequent down-regulation of genes involved in the p53 and apoptotic pathways, potentially contributing to tumor progression.

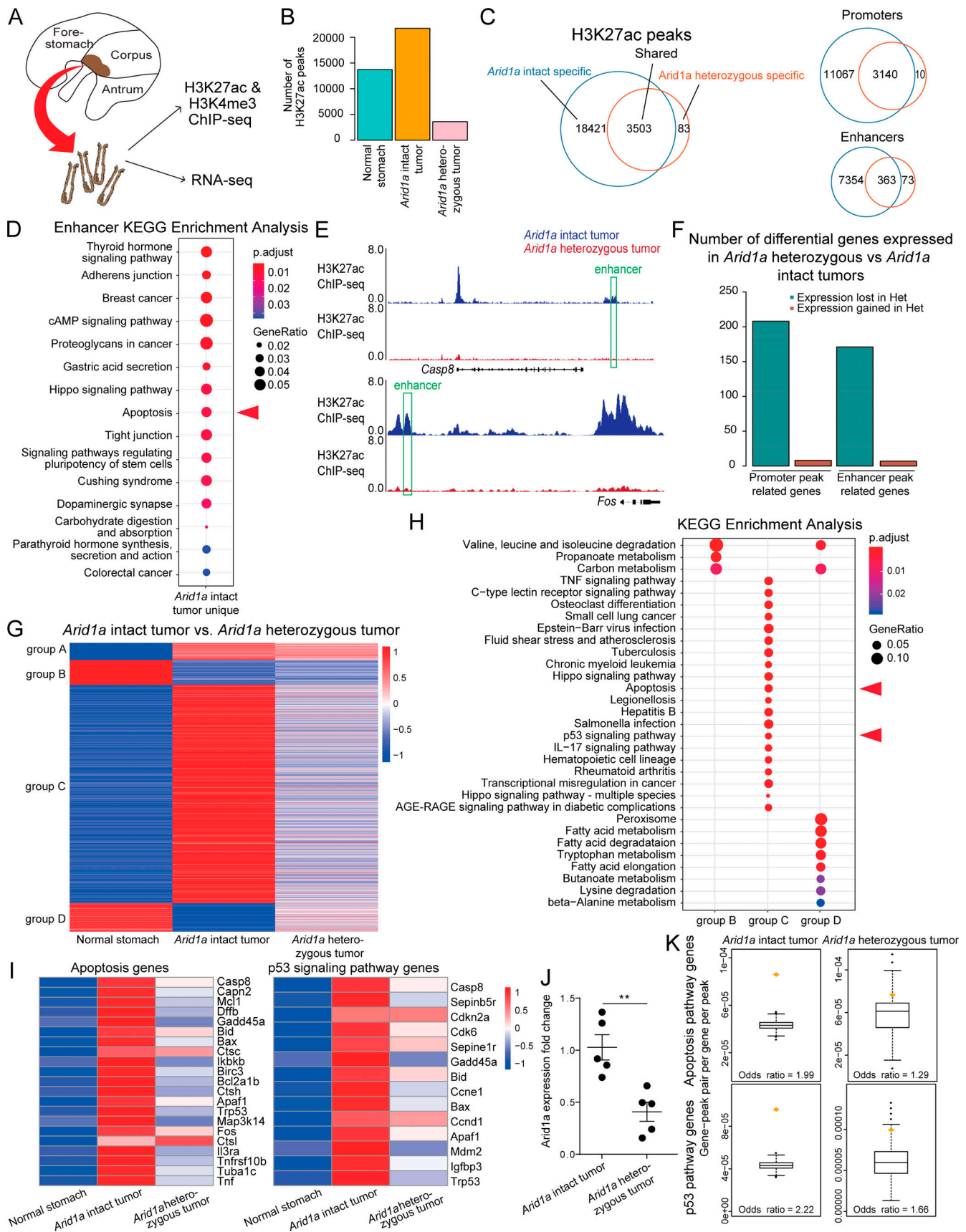


Figure 2. Chromatin and gene expression analyses of gastric adenomas with and without *Arid1a* heterozygosity. (A) Experimental overview of chromatin and transcriptomic analyses performed using normal (wild-type) stomachs and *Arid1a* intact and *Arid1a* heterozygous gastric tumors. (B) Analysis of

common H3K27ac peaks across replicates ($n = 2$ each) shows a drastic reduction in peak number in *Arid1a* heterozygous tumors compared with *Arid1a* intact tumors. **(C)** Venn diagrams outlining the number of H3K27ac marked peaks associated with enhancers and promoters that are common and unique to *Arid1a* intact and *Arid1a* heterozygous tumors. **(D)** Kyoto Encyclopedia of Genes and Genomes (KEGG) pathway enrichment analysis of enhancer elements unique to *Arid1a* intact tumor exhibits an enrichment in loci associated with apoptosis (red arrowhead). For *Arid1a* intact-specific enhancers, the top 2,000 enhancer peaks were used for analysis. **(E)** H3K27ac ChIP-seq-derived peak tracks of genes involved in apoptosis display a loss in peak signal at enhancer regions of *Arid1a* heterozygous tumors compared with *Arid1a* intact counterparts. Enhancer regions are outlined by a green box. **(F)** Analysis of the number of dysregulated genes that lose enhancer- and promoter-specific H3K27ac in *Arid1a* heterozygous tumors compared with *Arid1a* intact tumors. **(G)** A global heatmap of all the dysregulated genes between wild-type stomachs ($n = 3$), *Arid1a* intact tumors ($n = 3$), and *Arid1a* heterozygous tumors ($n = 3$) identifies four groups of dysregulated genes. Groups A and B are genes up-regulated and down-regulated in all tumor samples, respectively, regardless of *Arid1a* status. Group C comprises genes up-regulated in *Arid1a* intact tumors only, and group D comprises genes that are only down-regulated in *Arid1a* intact tumors. **(H)** KEGG pathway enrichment analysis of the four groups does not enrich for any specific pathways in group A, but apoptosis and p53 signaling are uniquely enriched in group C (red arrowheads). AGE, advanced glycation end products; RAGE, receptor for advanced glycation end products. **(I)** A higher-resolution heatmap of p53 signaling pathway and apoptosis-related genes highlights the up-regulation of these genes in *Arid1a* intact but not *Arid1a* heterozygous tumors when compared with wild-type gastric tissue. **(J)** RT-qPCR of *Arid1a* expression in the epithelial cells of *Arid1a* heterozygous tumors compared with *Arid1a* intact tumors confirms down-regulation of *Arid1a* (**, $P = 0.01$, unpaired t test). Bars represent mean \pm SEM. **(K)** Enrichment analysis of the overlap between H3K27ac signal and the enhancers of apoptosis and p53 signaling pathway genes shows an increased overlapping odds ratio for *Arid1a* intact tumors ($n = 2$) compared with *Arid1a* heterozygous tumors ($n = 2$). The orange diamond shows the true overlap between H3K27ac signal and the enhancers in each condition, and the box plot indicates background overlap.

To examine possible alternative mechanisms, we further analyzed the nature of ARID1A mutations found in human GC molecular subtypes. ARID1A mutations have been shown to be enriched in the genomically stable subtype of human GC, while TP53 mutations are enriched in the chromosomal instability subtype (The Cancer Genome Atlas Research Network, 2014). Since many human GC samples heterozygous for ARID1A harbor TP53 mutations (Fig. S2 L), we examined the relationship between the *Arid1a* deletion in our model and genome stability. Since mismatch repair is known to be important for maintaining genome stability (Li, 2008), we performed gene set enrichment analysis of mismatch repair pathways using our RNA-seq data. We found a significant enrichment of the mismatch repair pathway in *Arid1a* intact tumors compared with normal stomachs, while there was no significant enrichment or depletion of mismatch repair genes in *Arid1a* heterozygous tumors when compared with *Arid1a* intact tumors (Fig. S2 M). PCR analysis using a panel of high-sensitivity mononucleotide repeat loci did not identify high levels of microsatellite instability in either *Arid1a* intact or *Arid1a* heterozygous tumors (Fig. S2 N; Bacher et al., 2005). These findings suggest that both Notch-activated gastric adenomas, with or without single-copy *Arid1a* deletion, do not confer genomic instability associated with dysregulation of mismatch repair.

***Arid1a* plays cell type-specific roles during adult gastric homeostasis**

The reported roles of *Arid1a* in the gastrointestinal tract are highly tissue specific: deletion of *Arid1a* in the colon led to adenoma development, while *Arid1a* loss in the small intestine depleted stem cells and disrupted villi formation but did not form tumors (Hiramatsu et al., 2019; Mathur et al., 2017). Therefore, we also addressed the role of *Arid1a* during epithelial homeostasis in the adult stomach. Costaining of ARID1A with markers of parietal cells (H^+K^+ -ATPase), proliferating cells (proliferating cell nuclear antigen [PCNA]), pit cells (periodic acid-Schiff [PAS]), and chief cells (intrinsic factor) in the gastric epithelium showed that it is expressed ubiquitously in both differentiated and progenitor cells (Fig. S3, A–D).

To examine the role of *Arid1a* in adult gastric homeostasis, we conditionally deleted one or both copies of *Arid1a* in gastric parietal cells (*Atp4b*^{Cre};*Arid1a*^{fllox/+} and *Atp4b*^{Cre};*Arid1a*^{fllox/fllox}). Costaining of ARID1A and H^+K^+ -ATPase showed the specific deletion of *Arid1a* in parietal cells (Fig. S3 E). While we observed no abnormal phenotypes at 10 wk, histological analysis of mutant mice revealed regions of foveolar hyperplasia in the corpus of *Arid1a* homozygous mice but not heterozygous or *Cre*[−] mice at 25 wk (Fig. 3 A and Fig. S3 F). These features of foveolar hyperplasia include a basal restriction of H^+K^+ -ATPase⁺ parietal cells and a caudal extension of surface pit cells (Petersen et al., 2017). PAS staining for pit cells and immunofluorescence staining for parietal cells confirmed hyperplastic features (Fig. 3, B and C). Although Ki67 antibody staining showed an increased number of proliferating cells in the corpus of both *Arid1a* heterozygous and *Arid1a* homozygous mice, we observed no adenoma formation (Fig. 3, D and E). Since p53 signaling and apoptosis are suppressed in *Arid1a* heterozygous tumors, we also analyzed cleaved caspase-3 and p53 staining in *Arid1a* heterozygous and *Arid1a* homozygous mice. We did not identify any changes in cleaved caspase-3 protein expression between *Cre*[−] controls and mutants, and we found no visible expression of p53 protein in mutant mice (Fig. S3, G and H). This finding indicates that *Arid1a* is required to maintain adult gastric homeostasis, but its partial or complete loss in parietal cells does not efficiently drive tumor initiation.

MIST1 not only is a marker of mature chief cells found at the base of gastric glands but also has been shown to label quiescent stem cells that can act as the cell of origin for GC (Hayakawa et al., 2015; Stange et al., 2013). We confirmed Mist1-Cre expression by short-term tamoxifen studies (Fig. S3 I). To determine if *Arid1a* loss in MIST1⁺ cells can drive tumor initiation, we also generated mice with one or both copies of *Arid1a* deleted in MIST1⁺ cells (*Mist1*^{CreERT2};*Arid1a*^{fllox/+} and *Mist1*^{CreERT};*Arid1a*^{fllox/fllox}). At 6 wk post-induction (w.p.i.), a large number of corpus epithelial cells were depleted of ARID1A (Fig. S3 J). Interestingly, we identified rare foci of abnormal cystlike structures in the gastric epithelium of both heterozygous and homozygous mice (Fig. 3 F). These foci were also depleted of parietal cells, but they

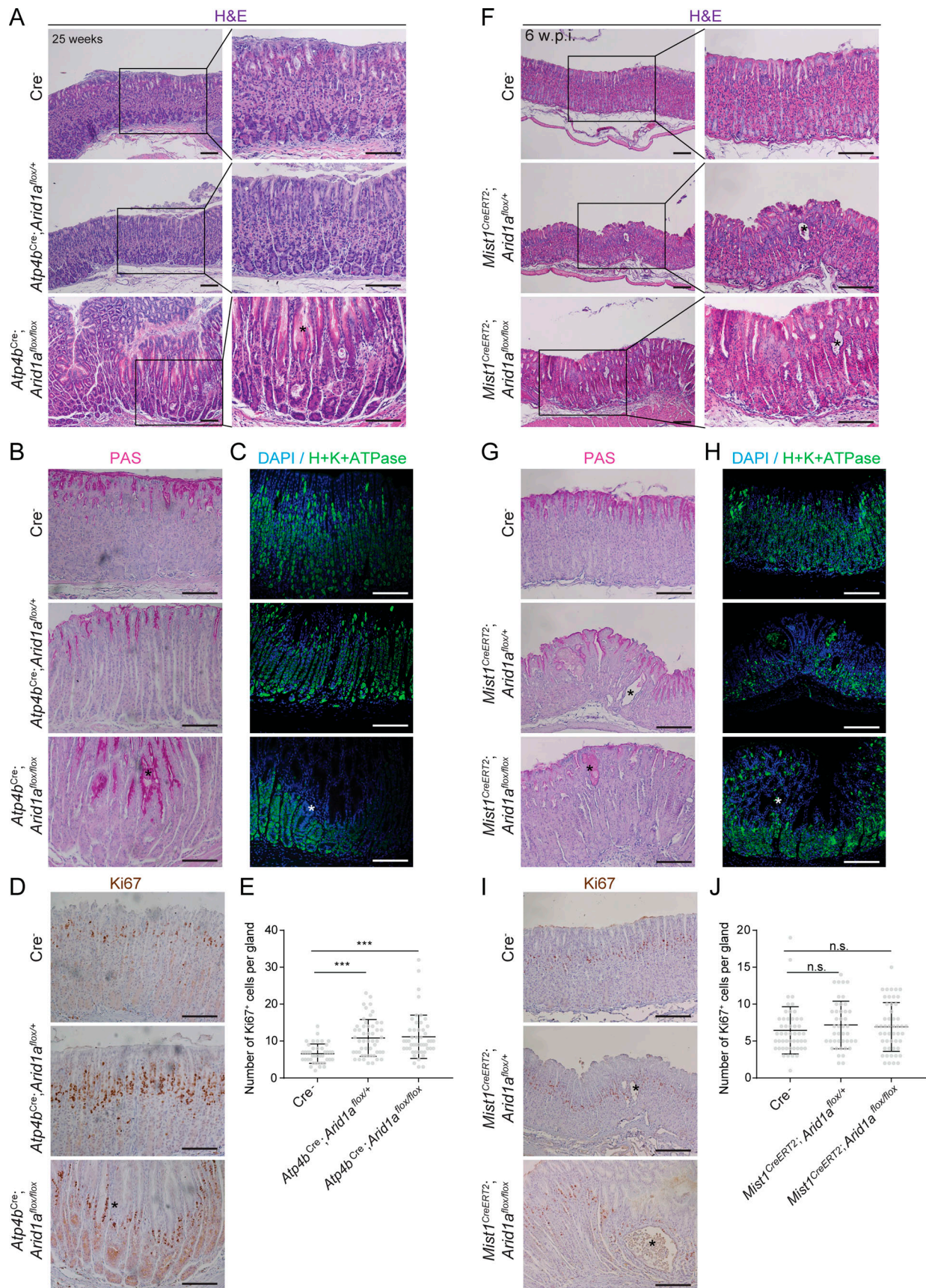


Figure 3. **The role of Arid1a in adult stomach homeostasis. (A)** Parietal cell-specific *Arid1a* deletion in aged mice exhibits regions of hyperplasia at 25 wk when compared with wild-type and *Arid1a* heterozygous mice. Asterisk marks the hyperplastic region ($n = 3$ each). Scale bar, 100 μm . **(B)** Representative

images of PAS staining of the stomach epithelia reveal basal extension of PAS⁺ cells in the hyperplastic regions of the *Arid1a*-deleted mice. Asterisk marks PAS⁺ hyperplastic regions in mutant samples ($n = 3$ each). Scale bar, 100 μm . (C) Representative immunofluorescence images of H⁺-K⁺-ATPase staining of the gastric epithelium shows a loss of H⁺-K⁺-ATPase⁺ parietal cells in the hyperplastic regions of *Atp4b*^{Cre};*Arid1a*^{lox/lox} mice, labeled by the asterisk ($n = 3$ each). Scale bar, 100 μm . (D) Representative images of Ki67 staining in the gastric epithelia ($n = 3$ each). Scale bar, 100 μm . (E) Quantification of Ki67 staining shows an increase in the number of proliferative cells in *Atp4b*^{Cre};*Arid1a*^{lox/+} and *Atp4b*^{Cre};*Arid1a*^{lox/lox} mice compared with *Cre*⁻ controls (***, $P < 0.001$, unpaired t test). Bars represent mean \pm SEM. (F) Deletion of either one copy or both copies of *Arid1a* in MIST1⁺ cells 6 w.p.i. leads to the formation of cystic structures (marked by asterisk). These cystic structures are not found in the injected *Cre*⁻ controls ($n = 3$ each). Scale bar, 100 μm . (G) Representative images of PAS staining did not identify extension of PAS⁺ cells along the cystic glands ($n = 3$ each). Scale bar, 100 μm . (H) Representative images of H⁺-K⁺-ATPase staining show the loss of parietal cells in the aforementioned cystic regions ($n = 3$ each). Scale bar, 100 μm . (I) Representative images of Ki67 staining in the gastric epithelium ($n = 3$ each). Scale bar, 100 μm . (J) Quantification of Ki67 staining shows no significant changes in the number of proliferative cells in *Mist1*^{CreERT2};*Arid1a*^{lox/+} or *Mist1*^{CreERT2};*Arid1a*^{lox/lox} compared with injected controls (unpaired t test). Bars represent mean \pm SEM.

did not display signs of foveolar hyperplasia, indicated by the restriction of PAS staining to the pit of the glands (Fig. 3, G and H). Consistently, we were unable to identify any significant increase in the number of Ki67⁺ proliferative cells (Fig. 3, I and J). We were also unable to detect apoptotic or p53⁺ cells in the abnormal glands (Fig. S3, K and L). Taken together, these experiments suggest that while the partial loss of *Arid1a* is sufficient to significantly promote tumor progression in the Notch signaling-activated adenoma model, its deletion alone in parietal cells or MIST1⁺ cells does not seem to efficiently drive tumor initiation.

***Arid1a* homozygous deletion confers competitive disadvantage through up-regulation of the p53 apoptotic pathway**

Only a small subset of patients within the available TCGA GC cohort displayed homozygous deletion of *Arid1a*, implying its dose-dependent roles in a clinical setting (Fig. 1 D). To determine if the homozygous deletion of *Arid1a* also promotes gastric tumor progression, we deleted both copies of *Arid1a* alleles in our gastric adenoma model (*Atp4b*^{Cre};*Rosa26*^{NICD};*Arid1a*^{lox/lox}). Interestingly, while immunofluorescence staining revealed an efficient deletion of *Arid1a* at early stages, ARID1A⁻ cells were progressively outcompeted by ARID1A⁺ *Cre* escaper cells at advanced stages (Fig. 4, A and B). To assess if ARID1A⁺ escaper cells may exhibit stem cell-like traits and confer a selective growth advantage within *Arid1a* homozygous tumors, we stained for a GC stem cell marker, CD44 (Takaishi et al., 2009). Interestingly, both ARID1A⁺ and ARID1A⁻ cells expressed CD44 (Fig. S4 A), suggesting that alternative mechanisms might be at play in attributing a fitness advantage to escaped tumor cells.

To further elucidate the mechanisms underlying the survival advantage of ARID1A⁺ versus ARID1A⁻ cells, we performed single-cell RNA-seq (scRNA-seq) on epithelial cells isolated from late-stage *Atp4b*^{Cre};*Rosa26*^{NICD};*Arid1a*^{lox/lox} tumors (Fig. 4 C). Consistent with our in vivo data, immunofluorescence staining for ARID1A on the sorted epithelial cells (Epcam⁺) showed both ARID1A⁺ and ARID1A⁻ cells (Fig. S4 B). Principal component analysis of the single-cell data revealed nine distinct clusters (Fig. 4 D). To determine the cell types represented by each cluster, we performed gene ontology (GO) enrichment for biological processes using the associated clustering markers (Fig. S4 C and Table S4). While cluster 0 and cluster 6 were enriched for terms related to proliferation and active cell division, multiple terms related to apoptosis were enriched in cluster 2. Terms

related to hypoxia were enriched in clusters. By categorizing each cluster based on *Arid1a* expression level, we identified two clusters (clusters 2 and 3) that had lower expression of *Arid1a* than the remaining clusters, which we termed the “*Arid1a*^{low} clusters” (Fig. 4 E). These clusters would likely represent cells that lost both copies of *Arid1a*.

By performing pathway enrichment analysis on the top markers of the *Arid1a*^{low} clusters, we found an enrichment of the p53 signaling pathway (Fig. 4 F). Analysis of the GO terms related to apoptosis also showed an increase in association with markers for clusters 2 and 3 compared with other cluster markers (Fig. S4 D). To further examine the correlation between p53 signaling and *Arid1a* expression in a single tumor, we analyzed the expression of various p53 signaling target genes. Expression levels of various players in the p53 pathway, such as *Cdkn1a*, *Cdkn2a*, *Bax*, *Igfbp3*, and *Ccng1*, were also found to be up-regulated in the *Arid1a*^{low} clusters compared with the *Arid1a*^{high} clusters (Fig. 4 G). Therefore, we conclude that the loss of fitness in tumors with *Arid1a* homozygous deletion is likely due to the activation of the p53 apoptotic pathway. Corroborating these data, *Trp53* expression was enriched in the *Arid1a*^{low} cluster cells (Fig. S4 E). To confirm that the *Arid1a*^{low} cells indeed have increased apoptosis, we performed immunofluorescence staining for ARID1A and Tdt-mediated dUTP-biotin nick end labeling (TUNEL) and found more apoptotic cells that were ARID1A⁻ than were ARID1A⁺ (Fig. 4, H and I). Consistent with the decrease in number of ARID1A⁻ cells during tumor progression, we found a reduced number of apoptotic cells in 20-wk-old *Arid1a* homozygous tumors compared with those found in 10-wk-old *Arid1a* homozygous tumors (Fig. S4, F and G). These data suggest that tumor cells continuing to express ARID1A possess a selective advantage over ARID1A⁻ cells.

To explore the molecular mechanism of p53 activation in ARID1A⁻ tumor cells, we performed H3K27ac ChIP-seq with gastric epithelial cells isolated from *Atp4b*^{Cre};*Rosa26*^{NICD};*Arid1a*^{lox/lox} mice at 10 wk, when the majority of cells are ARID1A⁻ (Fig. 4 A). We found that while there is a global reduction of H3K27ac peaks in *Arid1a* homozygous tumors compared with *Arid1a* intact tumors, there is an increased number of H3K27ac peaks when compared with *Arid1a* heterozygous tumors (Fig. 4 J and Fig. S4 H). We then isolated H3K27ac peaks associated with enhancers in *Arid1a* homozygous tumors and compared them with the enhancer peaks in *Arid1a* heterozygous tumors (Table S5). Notably, we found that a subset of enhancer peaks associated with p53 signaling and apoptosis genes, which

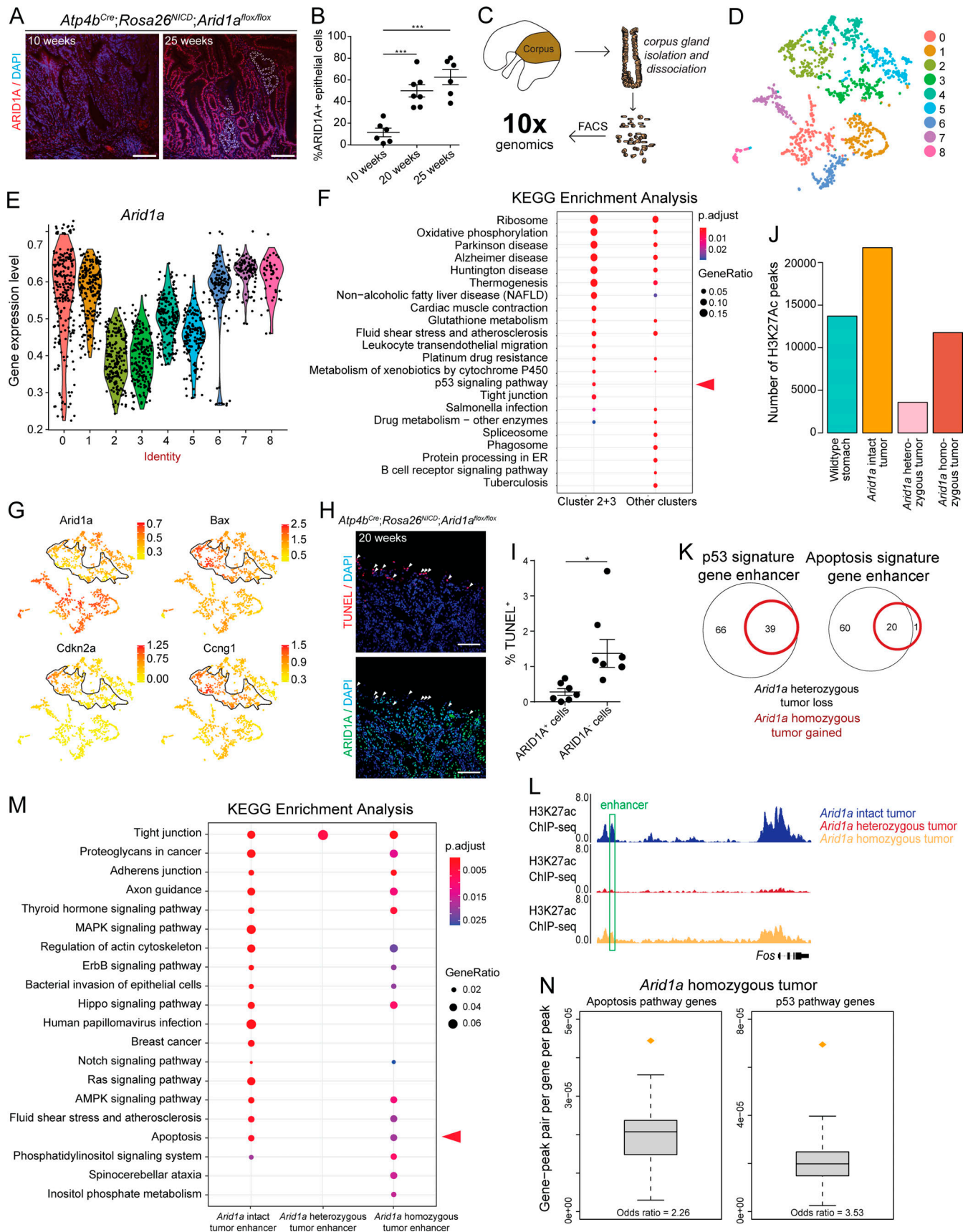


Figure 4. **Single-cell analysis of *Arid1a*-knockout gastric adenoma epithelium.** (A) Immunofluorescence images of ARID1A staining in *Arid1a*-deleted gastric adenomas at early and late stages ($n = 6-7$ each) demonstrate repopulation of adenomatous glands by ARID1A⁺ cells at 25 wk. The white dotted line

outlines the epithelium without ARID1A staining in late-stage tumors. Scale bar, 100 μm . **(B)** Quantification of the percentage of ARID1A⁺ epithelial cells at different stages confirms a progressive increase of ARID1A⁺ cells over time (***, $P = 2.2 \times 10^{-4}$ between 10 wk and 20 wk and $P = 8.5 \times 10^{-5}$ between 10 wk and 25 wk, unpaired *t* test). Bars represent mean \pm SEM. **(C)** Experimental overview of single-cell analysis of gastric adenomas with *Arid1a* deletion at a late stage of tumor progression. **(D)** Clustering analysis of scRNA-seq data from *Arid1a*-deleted gastric adenomas identifies nine clusters of cells with distinct expression profiles. **(E)** Violin plots depicting *Arid1a* expression among the nine clusters of cells identifies clusters 2 and 3 to have lower *Arid1a* expression than the other clusters. **(F)** Kyoto Encyclopedia of Genes and Genomes (KEGG) pathway enrichment analysis of clustering markers found an enrichment of the p53 signaling pathway (red arrowhead) in clusters 2 and 3 but not in the other clusters. **(G)** Feature plots of the scRNA-seq data show a negative correlation between *Arid1a* expression and the expression of genes related to p53 signaling and apoptosis (dotted line outlines *Arid1a*^{low} clusters). **(H)** Representative images of TUNEL and ARID1A immunofluorescence staining in *Arid1a* homozygous gastric adenomas; white arrowheads indicate TUNEL⁺ ARID1A⁻ cells ($n = 7$). Scale bar, 100 μm . **(I)** Quantification of TUNEL⁺ cells confirms an increase in the percentage of TUNEL⁺ cells in the ARID1A⁻ cell population compared with the ARID1A⁺ cell population (*, $P = 0.024$, paired *t* test). Bars represent mean \pm SEM. **(J)** Analysis of common H3K27ac peaks across replicates ($n = 2$ each) shows an increase in peak number in *Arid1a* homozygous tumors compared with *Arid1a* heterozygous tumors. **(K)** Among all the enhancers associated with p53 signaling and apoptosis genes that lost H3K27 acetylation in *Arid1a* heterozygous tumors (black circle), a subset of these enhancers was reactivated in *Arid1a* homozygous tumors when compared with *Arid1a* intact tumors (red circle). **(L)** Representative H3K27ac ChIP-seq track of an apoptosis-related gene, *Fos*, with loss in peak signals at enhancer regions of *Arid1a* heterozygous tumors compared with *Arid1a* intact and reactivation of peak signals in *Arid1a* homozygous tumors. Enhancer regions are outlined by a green box. **(M)** KEGG pathway enrichment analysis of enhancer H3K27ac peaks shows enrichment of apoptosis in *Arid1a* intact and *Arid1a* homozygous tumors but not in *Arid1a* heterozygous tumors (red arrowhead). AMPK, 5'-AMP-activated protein kinase. **(N)** Enrichment analysis of the overlap between H3K27ac signal and the enhancers of apoptosis and p53 signaling pathway genes shows an increased overlapping odds ratio for *Arid1a* homozygous tumors. The orange diamond shows the true overlap between H3K27ac signal and the enhancers in each condition, and the box plot indicates background overlap.

are absent in *Arid1a* heterozygous tumors compared with *Arid1a* intact tumors, are reactivated in *Arid1a* homozygous tumors (Fig. 4, K and L). Similarly, pathway enrichment analysis showed that the apoptotic pathway is enriched in *Arid1a* intact and *Arid1a* homozygous tumors but not *Arid1a* heterozygous tumors (Fig. 4 M). Moreover, there was a significant overlap between the H3K27ac peaks in *Arid1a* homozygous tumors and enhancers of apoptosis/p53 pathway genes that were not observed in *Arid1a* heterozygous tumors (Fig. 4 N).

To further analyze any changes in apoptosis between *Arid1a* heterozygous and *Arid1a* homozygous tumors, we performed TUNEL staining for tumors at 10 wk. We observed a trend of increased apoptotic cells without significance in *Arid1a* homozygous tumors when compared with *Arid1a* heterozygous tumors (Fig. S4, I and J). Consistent with this trend, within *Arid1a* homozygous tumors, we observed a significant increase in apoptosis in ARID1A⁻ tumor cells compared with escaped ARID1A⁺ tumor cells (Fig. 4, H and I). This difference in survival would likely increase the number of ARID1A⁺ cells over time (Fig. 4 B). Taken together, these experiments show that the complete deletion of *Arid1a* in tumor cells leads to enhancer activation and the up-regulation of apoptotic/p53 pathway genes, which may underlie the competitive disadvantage observed in ARID1A⁻ tumor cells.

Since ARID1A and ARID1B serve as mutually exclusive subunits of the BAF complex (Wu et al., 2014), we asked if the loss of *Arid1a* is compensated by an increase in *Arid1b* expression. By analyzing our RNA-seq data, we found no significant differences in *Arid1b* expression in *Arid1a* heterozygous tumors compared with *Arid1a* intact tumors (Fig. S4 K). In addition, analysis of scRNA-seq data showed no obvious changes in *Arid1b* expression between *Arid1a*^{low} clusters and *Arid1a*^{high} clusters (Fig. S4 L). To assess ARID1B expression in ARID1A⁻ cells, we performed ARID1A and ARID1B staining of serial sections and found that ARID1B is indeed expressed in both ARID1A⁻ and ARID1A⁺ regions in *Arid1a* homozygous tumors (Fig. S4 M). Together, these data suggest that the loss of *Arid1a* does not alter *Arid1b* gene expression in our gastric adenoma model.

Trp53 deletion rescues fitness disadvantage in ARID1A⁻ cells and promotes tumor invasion

To functionally determine if p53 signaling is required to drive the competitive disadvantage observed in ARID1A⁻ cells in vivo, we conditionally deleted both *Trp53* and *Arid1a* in our adenoma model (*Atp4b*^{Cre};*Rosa26*^{NICD};*Trp53*^{fllox/fllox};*Arid1a*^{fllox/fllox}). Immunofluorescence staining of ARID1A in the tumors showed that loss of *Trp53* significantly recovers the population of ARID1A⁻ tumor cells, demonstrating a partial rescue of fitness disadvantage in ARID1A⁻ cells (Fig. 5, A and B; and Fig. S5 A). Interestingly, we found that while single mutants bear tumors contained in the lumen of the stomach, some *Trp53*^{-/-} *Arid1a*^{-/-} mice have visible tumors outside of the stomach, suggesting the presence of invasion (Fig. 5 C). Furthermore, while none of the *Arid1a* single mutants analyzed contained invasive tumors, 20% (2 of 10) of double-mutant mice showed early signs of invasion (classified as T1a), and 30% (3 of 10) had tumors that invaded the submucosa (termed “T4”; Fig. 5, D and E). Costaining of ARID1A and the epithelial cell marker, E-cadherin, in the regions of submucosal invasion of *Atp4b*^{Cre};*Rosa26*^{NICD};*Trp53*^{fllox/fllox};*Arid1a*^{fllox/fllox} mice showed that most E-cadherin⁺ tumor cells were ARID1A⁻, suggesting that *Trp53* deletion in *Arid1a*-deleted cells promoted their invasiveness (Fig. S5 B).

To further investigate the effect of *Arid1a* and *Trp53* deletion on tumor cell growth, we established organoids using glands isolated from *Arid1a* homozygous tumors and *Arid1a* and *Trp53* doubly deleted tumors, and we found no significant differences in the size of organoids formed (Fig. S5, C and D). The culture media, supplemented with various growth factors, might have masked their potential difference in vitro. To determine if the concurrent deletion of *Arid1a* and *Trp53* is able to drive tumor formation in differentiated gastric epithelial cells, we simultaneously deleted *Arid1a* and *Trp53* in parietal cells (*Atp4b*^{Cre};*Trp53*^{fllox/fllox};*Arid1a*^{fllox/fllox}). Histological analysis of the stomachs of these mice at 25 wk identified abnormal gland structures (Fig. S5 E). Although we observed a trend of increased disease scores in *Arid1a*;*Trp53* double mutants compared with *Arid1a* single mutants (Fig. S5 F), we found no dysplasia in the mutants,

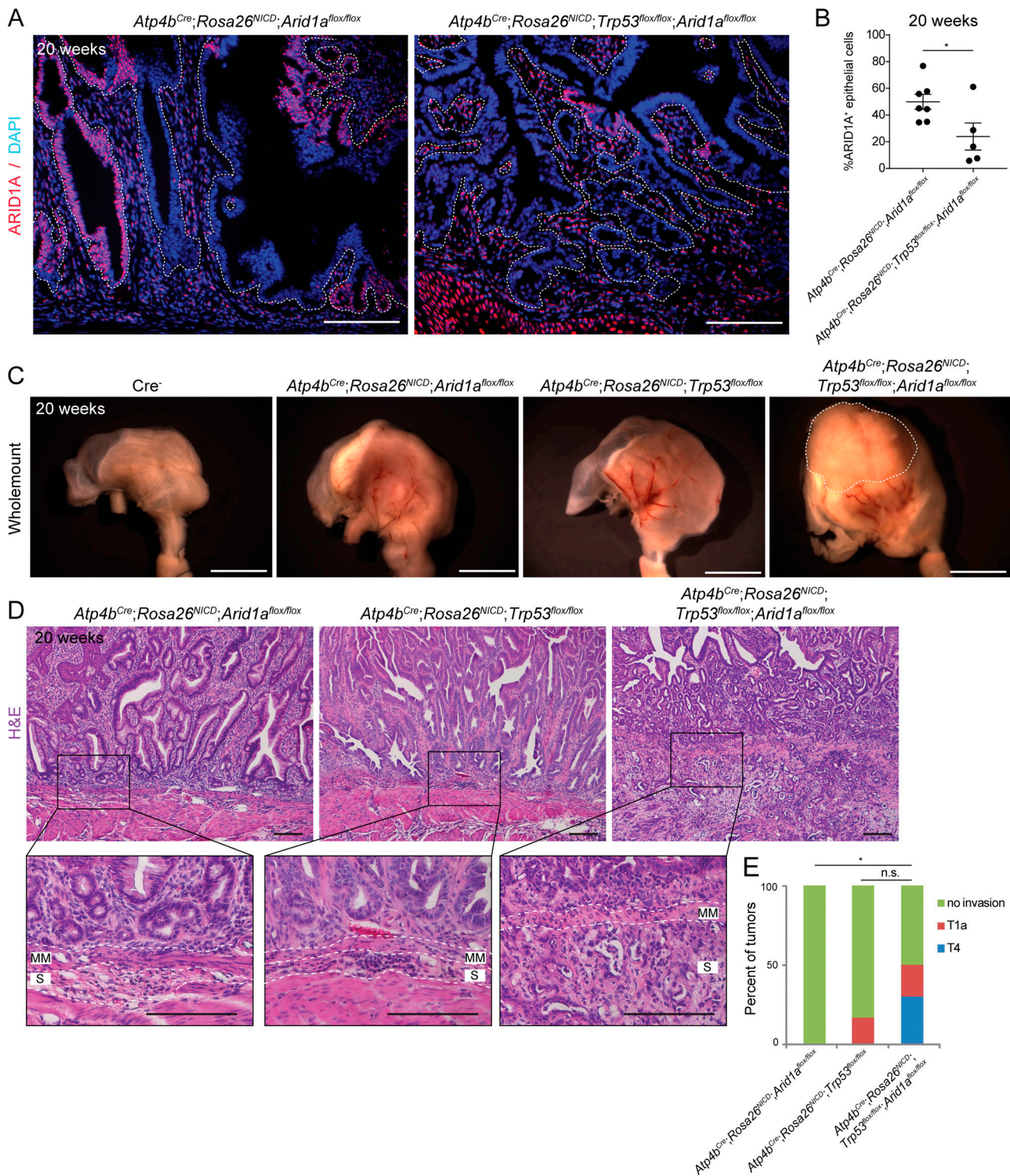


Figure 5. Analysis of Trp53 and Arid1a interaction during gastric tumor progression. (A) Representative immunofluorescence images of ARID1A staining in gastric adenomas with the deletion of *Arid1a* alone or *Arid1a* and *Trp53* together; the white dotted lines outline the boundary between the epithelium and mesenchyme ($n = 5-7$ each). Scale bar, 100 μm . **(B)** Quantification of ARID1A-expressing cells in the adenomatous epithelium confirms a significant reduction in ARID1A⁺ cells in *Arid1a* and *Trp53* doubly deleted tumors compared with *Arid1a* deleted tumors (*, $P = 0.036$, unpaired t test). Bars represent mean \pm SEM. **(C)** Whole-mount images of stomachs from mice with single or double deletion of *Arid1a* and *Trp53*; the white dotted line demarcates the protrusion found in the stomach of mice with *Arid1a* and *Trp53* double deletion. Scale bar, 5 mm. **(D)** Representative histological images of the gastric layers from mice with single or double deletion of *Arid1a* and *Trp53*, highlighting an example of submucosal invasion in the doubly deleted mice; the white dotted line demarcates the muscularis mucosa (MM) and the submucosa (S). Scale bar, 100 μm . **(E)** Quantification of the percentage of invasive tumors demonstrates increased incidents of invasion in *Arid1a*/*Trp53* doubly deleted tumors compared with *Arid1a* singly deleted or *Trp53* singly deleted tumors ($n = 10$, $n = 7$, and $n = 6$, respectively; *, $P = 0.026$ between *Arid1a* single mutant and double mutant; n.s., $P = 0.18$ between *Trp53* single and double mutants, χ^2 test for the occurrence of invasion including T1a and T4).

suggesting that *Trp53* deletion may not be able to efficiently drive tumor formation in *Arid1a*-deleted parietal cells.

Combined therapy targeting both the BAF complex and the p53 pathway

Given the loss of fitness observed in *ARID1A*⁻ cells, we hypothesized that further disruption of the BAF complex would inhibit the growth of *Arid1a* heterozygous tumor cells. The epigenetic inhibitor, TPO64, has recently been identified to be an inhibitor of CARM1, which regulates the methylation of the core BAF complex subunit, BAF155 (Nakayama et al., 2018). This methylation was shown to direct the complex to chromatin regions associated with oncogenic genes (Wang et al., 2014). Therefore, we hypothesized that TPO64 may have therapeutic effects on *Arid1a* heterozygous tumors. To address this question, we treated gastric organoids established from tumor or normal (wild-type) stomach glands with TPO64 at 1.5 μ M and found significantly reduced size of *Arid1a* intact and *Arid1a* heterozygous tumor organoids compared with normal organoids (Fig. 6, A–C). In addition, to confirm if isolated *Arid1a* heterozygous tumor cells exhibit reduced *Arid1a* expression levels in tumor organoid culture, we conducted RT-qPCR on normal and tumor organoids before drug treatment. We found that *Arid1a* expression is significantly reduced in *Arid1a* heterozygous tumor organoids compared with either normal or *Arid1a* intact tumor organoids (Fig. S5 G).

Since, compared with *Arid1a* heterozygous tumors, genes up-regulated in *Arid1a* intact tumors were enriched for the p53 signaling pathway, we hypothesized that treatment with a p53 agonist may further inhibit the growth of *Arid1a* heterozygous tumor cells. To address this hypothesis, we treated gastric tumor organoids with both TPO64 and Nutlin-3, a well characterized p53 agonist (Vassilev et al., 2004). We found that while treatment of 1 μ M TPO64 and 1 μ M Nutlin-3 alone did not significantly alter the viability of normal or *Arid1a* heterozygous tumor organoids, their combined treatment had a synergistic effect in reducing the viability of these organoids (Fig. 6 D). When we treated the organoids with 1.5 μ M TPO64 and 2 μ M Nutlin-3, we found further reduction in organoid viability, with a significantly greater effect in *Arid1a* heterozygous tumor organoids compared with either normal or *Arid1a* intact tumor organoids (Fig. 6, D and E). The size of *Arid1a* heterozygous tumor organoids also was greatly reduced after 3 d of combinatorial treatment with TPO64 and Nutlin-3 (Fig. 6, F and G). To identify any changes in gene expression upon drug treatment at the concentrations used, we performed RT-qPCR and identified a number of p53 pathway genes, such as *Ccng1*, *p21*, and *Trp53*, that became up-regulated to a greater level after combinatorial treatment than with individual treatment alone (Fig. 6 H). Together, our work shows that the combined use of TPO64 and Nutlin-3 may synergistically activate the p53 pathway and inhibit the growth of *Arid1a* heterozygous gastric tumors.

Discussion

Although *ARID1A* is one of the most commonly mutated genes in GC, the functional effects of *ARID1A* mutations in GC have not

been addressed in vivo. Using our clinically relevant GC models and performing genomic and epigenomic profiling, we demonstrate in vivo that *Arid1a* heterozygosity in a *Notch*-activated gastric adenoma model sufficiently promotes tumor progression through the regulation of enhancers and genes involved in the p53 and apoptosis pathways.

Interestingly, the role of *Arid1a* is highly context and tissue dependent. *Arid1a* acted as a tumor suppressor in the colon but not in the small intestine (Mathur et al., 2017). However, loss of *Arid1a* delayed colon and ovarian cancer formation in the context of *Apc* mutations (Zhai et al., 2016). While pancreatic deletion of *Arid1a* alone initiated metaplastic and neoplastic lesions, these lesions only progressed to pancreatic ductal adenocarcinoma upon oncogenic cooperation with *KRAS* (Kimura et al., 2018; Wang et al., 2019). In the liver, *Arid1a* loss prevented tumor initiation, but *Arid1a* deletion in established tumors promoted cancer progression (Sun et al., 2017). Consistent with these data, while the heterozygous deletion of *Arid1a* in our gastric adenoma model promoted tumor progression, neither the *Arid1a* heterozygous deletion nor the *Arid1a* homozygous deletion in differentiated parietal cells and chief cells was able to efficiently initiate tumorigenesis.

Since Notch signaling is known to be activated in GC (Yao et al., 2017) and its activation in parietal cells induces their de-differentiation targeting all stomach gland cells (Kim and Shivdasani, 2011), we used a *Notch*-activated gastric adenoma model in our study to specifically target *Arid1a* in the stomach. We also found that the *Notch* pathway genes are frequently amplified, and their expression is increased in *ARID1A* mutant GC, supporting the human relevance of using our *Notch*-activated model. Several studies have shown that *MIST1* labels a slowly cycling stem cell population in the gastric corpus (Stange et al., 2013), and oncogenic mutations targeting *MIST1*⁺ cells lead to tumor initiation (Hayakawa et al., 2015). However, deletion of one or both copies of *Arid1a* in *MIST1*⁺ cells in the gastric epithelium was not able to efficiently drive tumor formation. Interestingly, a recent genomic and epigenomic profiling study showed that *ARID1A* is less frequently mutated in human intestinal metaplasia than in advanced GC (Huang et al., 2018). This finding is supportive of our result in which *Arid1a* loss alone may not efficiently initiate gastric tumorigenesis and requires oncogenic cooperation, such as that contributed by *Notch* signaling activation. Since inflammation is a critical step in gastric tumorigenesis (Correa and Piazuelo, 2012), diverse immune responses due to differences in genetic background between mouse strains may also contribute to variation in the tumor severity observed in our study.

To define the transcriptional and epigenetic mechanisms underlying *Arid1a* heterozygosity-mediated tumor progression, we performed H3K27ac/H3K4me3 ChIP-seq and RNA-seq experiments. Our genome-wide investigation revealed a significant global reduction in H3K27ac and H3K4me3 levels when *Arid1a* heterozygous loss was induced compared with *Arid1a* intact tumors. This surprising result suggests the importance of broad control of enhancer activity mediated by the BAF complex. Our GO analysis showed down-regulation of the p53 signaling and apoptotic pathway genes in *Arid1a* heterozygous tumors

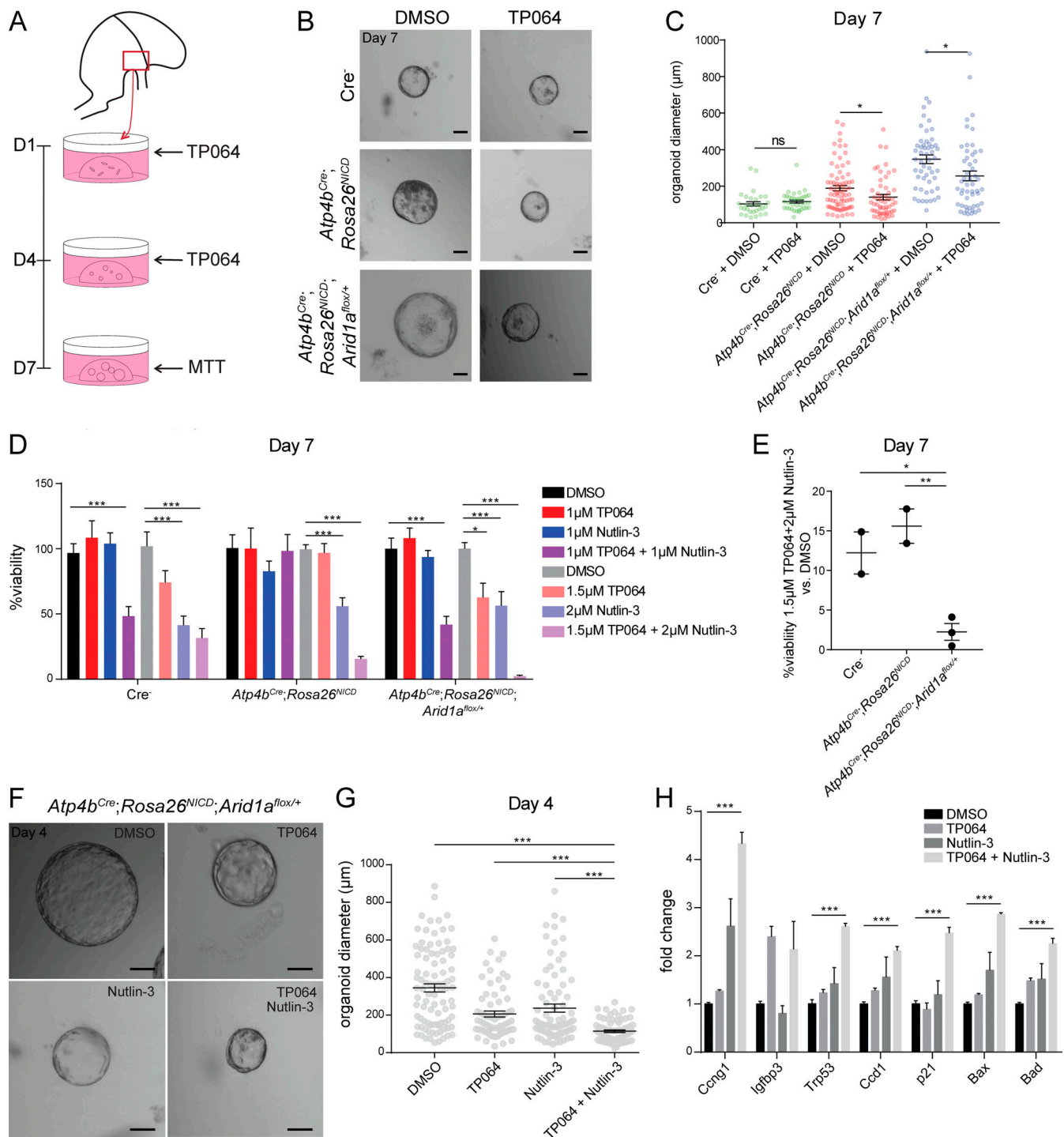


Figure 6. Combinatorial drug treatment of gastric tumor organoids. (A) Experimental overview of the small molecule treatment in gastric organoid culture. (B) Representative images of *Cre*⁻ wild-type, *Arid1a* intact tumor, and *Arid1a* heterozygous tumor organoids on day 7 after treatment with 1.5 μM TP064 or DMSO as a control. Experiments were repeated at least twice with organoids obtained from different mice for each genotype. Scale bar, 100 μm. (C) Quantification of organoid diameter on day 7 of treatment with 1.5 μM TP064 reveals a significant reduction in the size of *Arid1a* intact ($P = 0.022$, unpaired *t* test) and *Arid1a* heterozygous tumor organoids (*, $P = 0.012$, unpaired *t* test), but not of *Cre*⁻ wild-type organoids, compared with DMSO treatment. Bars represent mean ± SEM. (D) The viability of tumor organoids on day 7 of combinatorial or lone treatment using the indicated concentration of TP064 and/or Nutlin-3 versus DMSO demonstrates a synergistic reduction in organoid viability after combined treatment (*, $P < 0.05$; ***, $P < 0.001$; unpaired *t* test). Combinatorial but not individual treatment of TP064 and Nutlin-3 at 1 μM significantly inhibits the viability of *Cre*⁻ wild-type and *Arid1a* heterozygous tumor organoids, thus supporting a synergistic effect of the two small molecules. Organoid viability is further reduced with combinatorial treatment of 1.5 μM TP064 and 2 μM Nutlin-3. Each drug treatment was repeated with organoids established from at least two different mice for each genotype, and each biological replicate was treated with the same condition in at least three different wells. Error bars represent SEM. (E) Combinatorial treatment of 1.5 μM TP064 and 2 μM Nutlin-3 exhibits greater inhibition of viability in *Arid1a* heterozygous tumor organoids than *Cre*⁻ wild-type organoids and *Arid1a* intact tumor organoids.

Each data point represents the average percentage viability of an individual set of experiments using organoids established from a different mouse (*, $P < 0.05$; **, $P < 0.01$). Bars represent mean \pm SEM. **(F)** Representative images of *Arid1a* heterozygous tumor organoids on day 4 of combinatory treatment of 1.5 μ M TP064 and/or 2 μ M Nutlin-3 or DMSO. Experiments were repeated twice with organoids obtained from two different mice. Scale bar, 100 μ m. **(G)** Quantification of the diameter of *Arid1a* heterozygous tumor organoids after 4 d of treatment with either both 1.5 μ M TP064 and 2 μ M Nutlin-3 or separately shows a significant reduction in organoid size after simultaneous treatment of TP064 and Nutlin-3 compared with DMSO and single-compound treatment. Experiments were repeated twice with organoids obtained from two different mice (***, $P < 0.001$; unpaired *t* test). Bars represent mean \pm SEM. **(H)** RT-qPCR analysis of *Arid1a* heterozygous tumor organoids on day 4 of treatment with DMSO, 1.5 μ M TP064, 2 μ M Nutlin-3, or both 1.5 μ M TP64 and 2 μ M Nutlin-3 shows significant up-regulation of p53 signaling and apoptosis genes after simultaneous treatment of TP064 and Nutlin-3 compared with DMSO. Experiments were repeated twice with organoids obtained from two different mice (***, $P < 0.001$; unpaired *t* test). Error bars represent SEM.

compared with *Arid1a* intact tumors. Consistent with our data, the previous studies in gynecological cancers showed that ARID1A activates p53 target genes and promotes apoptosis (Bitler et al., 2017; Guan et al., 2011). Although we observed suppression of enhancers and genes involved in p53 signaling in *Arid1a* heterozygous tumors, apoptosis was moderately affected, suggesting that this epigenetic suppression gradually influences apoptosis over time, leading to increased tumor growth and progression.

In contrast to *Arid1a* heterozygosity-mediated down-regulation of the p53 and apoptosis pathways, our mouse genetic and single-cell analyses demonstrated that *Arid1a* homozygous deletion surprisingly confers a competitive disadvantage through the abnormal activation of the p53 apoptotic pathway. The reduced fitness of *Arid1a* homozygous cells may also explain the observation that poorly differentiated GCs have an increased level of ARID1A protein expression compared with moderately differentiated GCs (Fig. 1 B), as ARID1A⁻ cells may be eliminated in the later stages of cancer progression. This may be driven in part by the reactivation of enhancers associated with apoptotic genes that are inactivated in *Arid1a* heterozygous tumors. It has been proposed that the oncogenic effect of *Arid1a* loss is dependent on its mutually exclusive BAF complex subunit, Arid1b (Mathur et al., 2017). Therefore, in the absence of *Arid1a*, Arid1b may drive the reactivation of these enhancers. Consistently with the activation of p53 signaling in ARID1A⁻ cells, double deletion of *Arid1a* and *Trp53* in our tumor model not only partially rescued the competitive disadvantage of ARID1A⁻ cells but also facilitated tumor progression and invasion. Our data may explain the low number of GC patients harboring homozygous alterations of both ARID1A and TP53, as they may experience early lethality caused by aggressive cancer.

Collectively, our data not only highlight distinct dosage-dependent roles of *Arid1a* but also reveal a targetable vulnerability in *Arid1a* heterozygous tumors, suggesting that further disruption of the BAF complex may have therapeutic potential. Consistent with this notion, TP064, which inhibits CARM1, a key regulator of the BAF complex (Nakayama et al., 2018), suppressed the growth of *Arid1a* heterozygous tumor organoids. Since p53 signaling was activated in *Arid1a* heterozygous tumors, we hypothesized that p53 activation also would enhance its therapeutic effects. Indeed, we found that the cotreatment of TP064 with Nutlin-3, a p53 agonist currently in clinical trial, significantly improved the inhibition of the growth and viability of *Arid1a* heterozygous tumor organoids compared with individual treatment alone. This suggests that a combined approach of these small molecules may be a viable option in treating *Arid1a*

heterozygous GCs, which contribute to a large proportion of cases.

Materials and methods

Clinical samples and immunohistochemistry

Fifteen GC and five paracancerous formalin-fixed, paraffin-embedded samples were collected from the Department of Pathology, Second Hospital of Shandong University. The pathological grade of each sample was examined by pathological specialists. Immunohistochemistry was performed with a standard antigen retrieval protocol. Rabbit polyclonal anti-ARID1A antibody (Sigma-Aldrich; HPA005456) was used for immunohistochemistry. All stained slides were digitized with a NanoZoomer S60 Digital slide scanner (Hamamatsu Photonics; C13210-01). This study was reviewed and approved by the ethics committee of the Second Hospital of Shandong University with written informed consent received from all the patients.

Mouse experiments

All mouse experiments were performed in adherence to guidelines set forth by the Canadian Council on Animal Care and approved by The Centre for Phenogenomics. *Trp53^{fllox}* (stock no. 008462; Marino et al., 2000)/*Rosa26^{NICD1-Ires-GFP}* (stock no. 008159; Murtaugh et al., 2003) and *Atp4b^{Cre}* (stock no. 030656; Syder et al., 2004) mice were gifts from R. Shivdasani (Dana Farber Cancer Institute, Boston, MA), J. Mills (Washington University, St. Louis, MO), and C.C. Hui (Hospital for Sick Children, Toronto, ON, Canada). *Arid1a^{fllox}* (stock no. 027717; Gao et al., 2008) and *Mist1^{CreERT2}* (stock no. 029228) mice were purchased from The Jackson Laboratory. To generate *Atp4b^{Cre}*, *Arid1a^{fllox/+}* and *Atp4b^{Cre};Arid1a^{fllox/fllox}* mice, *Atp4b^{Cre}* mice were crossed to *Arid1a^{fllox}* mice and backcrossed for multiple generations to obtain the animals used in our experiments. *Atp4b^{Cre}* were first crossed to *Rosa26^{NICD1-Ires-GFP}*, and the *Atp4b^{Cre};Rosa26^{NICD1-Ires-GFP}* litters were crossed to *Arid1a^{fllox}*, which were then intercrossed for multiple generations to generate *Atp4b^{Cre};Rosa26^{NICD1-Ires-GFP}*, *Atp4b^{Cre};Rosa26^{NICD1-Ires-GFP};Arid1a^{fllox/+}*, and *Atp4b^{Cre};Rosa26^{NICD1-Ires-GFP};Arid1a^{fllox/fllox}* mice used for experiments. Similarly, *Trp53^{fllox}* mice were crossed to *Atp4b^{Cre};Rosa26^{NICD1-Ires-GFP}* mice and intercrossed to generate *Atp4b^{Cre};Rosa26^{NICD1-Ires-GFP};Trp53^{fllox/fllox}* mice, which were then crossed to *Arid1a^{fllox}* mice and intercrossed for multiple generations to generate the *Atp4b^{Cre};Rosa26^{NICD1-Ires-GFP};Trp53^{fllox/fllox}* and *Atp4b^{Cre};Rosa26^{NICD1-Ires-GFP};Trp53^{fllox/fllox};Arid1a^{fllox/fllox}* mice used for experiments. To activate Cre in *Mist1^{CreERT2}* mice, tamoxifen was injected intraperitoneally at 4 wk of age at 2 mg for 5

consecutive days. The mice were then dissected at 6 w.p.i. to match analysis with 10-wk-old mice.

Western blot analysis

Isolated gastric corpus epithelial cells were lysed in ice-cold lysis buffer (50 mM Tris-HCl, pH 7.5, 150 mM NaCl, 1 mM EDTA, 1% NP-40, 0.1% SDS, and 0.25% sodium deoxycholate) supplemented with 1 mM PMSF and protease inhibitor cocktail (Roche). The concentration of the isolated protein was determined using a detergent-compatible protein assay (Bio-Rad Laboratories). The samples were prepared by boiling in SDS loading buffer (100 mM Tris-HCl, pH 6.8, containing 4% SDS, 0.02% bromophenol blue, and 2% 2-mercaptoethanol). Whole-cell lysates were fractionated by SDS-PAGE and transferred to a nitrocellulose membrane (Bio-Rad Laboratories). The blotted membrane was blocked for 1 h in Tris-buffered saline with Tween 20 (10 mM Tris, pH 8.0, 150 mM NaCl, 0.5% Tween 20) containing 5% skim milk and then incubated with the primary antibodies against the ARID1A (Sigma-Aldrich; HPA005456) or GAPDH (Abcam; ab181602). Secondary peroxidase-labeled anti-mouse or anti-rabbit IgG antibodies were purchased from Thermo Fisher Scientific. Membranes were washed with Tris-buffered saline with Tween 20 and developed with Super-Signal West Pico Chemiluminescent Substrate (Thermo Fisher Scientific; 34080) using the ChemiDoc MP system (Bio-Rad Laboratories).

Immunofluorescence

Tissues were fixed in 4% PFA at 4°C overnight and embedded in paraffin. 5- μ m sections (adult) and 3- μ m sections (embryonic) were rehydrated through ethanol series. Antigen retrieval was performed in 10 mM sodium citrate, pH 6, using a microwave. Sections were blocked in 10% goat serum and incubated in primary antibody (1:200) overnight at 4°C (ARID1A, HPA005456, Sigma-Aldrich; H⁺-K⁺-ATPase, D032-3, MBL International Corporation; PCNA, sc-56, Santa Cruz Biotechnology; intrinsic factor, D. Alpers, Washington University). Sections were then washed thoroughly and incubated in secondary antibody (1:750) and DAPI for 1 h at room temperature. TUNEL staining was performed using the In Situ Cell Death Detection Kit, TMR red (Sigma-Aldrich; 12156792910) according to the manufacturer's protocol. Sections were washed thoroughly and mounted in Anti-Fade Fluorescence Mounting Media (Abcam; ab104135).

Immunohistochemistry

5- μ m sections were rehydrated through ethanol series. Antigen retrieval was performed in 10 mM sodium citrate, pH 6, using a microwave. Antigen retrieval was performed in 10 mM sodium citrate pH6 using a microwave. Sections were then treated with 3% H₂O₂ to remove endogenous peroxidase activities. Sections were blocked in 10% goat serum, followed by avidin and biotin. Sections were then incubated in primary antibody (1:500) overnight at 4°C (p53, NCL-L-p53-CM5p, Leica Biosystems; cleaved caspase-3, MilliporeSigma AB3623). Sections were then washed thoroughly and incubated in biotinylated secondary antibody for 1 h at room temperature (secondary antibody, 1:750), followed by avidin-biotin complex for 30 min, and

developed in DAB. Sections were counterstained in hematoxylin and dehydrated through an ethanol series.

PAS staining

5- μ m sections were rehydrated through ethanol series. Sections were stained using the PAS stain kit (StatLab; SSK-PAS[DIA-STASE]) according to the provided protocol.

Stomach gland isolation and RNA isolation

The corpus regions of the stomach that have tumors (or analogous regions in normal stomachs) were dissected and incubated in 20 mM EDTA for 30 min. The glands were then extracted by gently scraping the surface using a glass slide. The glands were washed thoroughly in PBS before downstream application. Isolated epithelial cells were immediately frozen, and RNA isolation was conducted using an RNA isolation kit (Qiagen; 74104).

ChIP-seq

Fresh epithelial pellets were fixed in 1% PFA for 10 min at room temperature, quenched with a 1/20th volume of 2.5 M glycine for 5 min, washed twice with cold 1 \times PBS, and flash frozen. When enough sample was acquired (~0.1 g of tissue per region), fixed pellets were pooled, dounced in cold PBS with protease inhibitor, and filtered through a 70- μ m mesh. Samples were then incubated in cold cell membrane and nuclear lysis buffers containing nondenaturing detergents for 30 min each on a shaker at 4°C. Washed samples were pelleted and resuspended in 300 μ l sonication buffer containing 0.1% SDS. Sonication was conducted using the Diagenode bioruptor (Diagenode; B01020001) at high power for 30 cycles, 30 s ON/OFF. Sonicated samples were cleared with a 1:10 dilution of 30% Triton X-100 and added to antibody-bound beads (rabbit anti-H3K27ac, ab4729; Abcam). The next day, beads were washed with high- and low-salt buffers and treated with proteinase K overnight at 65°C. DNA was isolated using phenol/chloroform extraction, and 10 ng immunoprecipitated DNA was used for cDNA library construction using the Rubicon DNA-seq Thruplex 48S kit. Libraries were size selected and submitted to be sequenced at 50-bp read length, single-end reads with 15–20 million reads per library.

ChIP-seq analysis

Single-end reads of H3K27ac and H3K4me3 ChIP-seq data were aligned to the GRCm38 mouse reference genome by Bowtie 2 with default parameters (Langmead and Salzberg, 2012). The aligned BAM files were then subjected to MASC2 for peak calling using “callpeak” mode with parameters “-keep-dup=1” and “--SPMR” (Zhang et al., 2008). ChIP-seq peaks were filtered by ENCODE mm10 blacklist regions (<https://www.encodeproject.org/annotations/ENCSR636HFF/>) for downstream analysis. The University of California Santa Cruz Genome Browser bedGraphToBigWig tool was used to convert resultant bedgraph files to big wiggle files for peak visualization in the Integrative Genomics Viewer (Robinson et al., 2011). The R packages “ChIPseeker” (Yu et al., 2015) and “clusterProfiler” (Yu et al., 2012) were used for the annotation and functional enrichment analysis of ChIP-seq peaks. Two replicates of H3K27ac ChIP-seq

were conducted for wild-type stomachs and for *Arid1a*-intact, *Arid1a*-heterozygous, and *Arid1a*-deleted gastric tumors. Only the common peaks of two replicates for each group were used for downstream analysis. To determine whether a subset of H3K27ac peaks was enriched in gene enhancer regions of a specific pathway, we first calculated the overlapping ratio of pathway gene enhancer regions with H3K27ac peaks and then compared the ratio with the genome background ratios, which were calculated by randomly sampling the same number of gene enhancer regions from all protein coding gene lists for 1,000 times.

RNA-seq analysis

Single-end RNA-seq reads were aligned to the GRCm38 mouse reference genome by STAR 2.4.2a (Dobin et al., 2013). The reads per kilobase per million mapped reads (RPKM) method was used to quantify gene expression of RNA-seq data. Differentially expressed genes were selected by the threshold of absolute fold change (RPKM + 1) > 1.5 and P < 0.05. The R package “clusterProfiler” (Yu et al., 2012) was used for the functional enrichment analysis of RNA-seq data.

TCGA data analysis

ARID1A genomic alteration status, TNM stages, and Notch pathway gene amplification status for TCGA Stomach Adenocarcinoma data collection (TCGA-STAD) samples were retrieved from cBioPortal (<https://www.cbioportal.org/>). 407 TCGA-STAD RNA-seq data were downloaded from the Genomic Data Commons Data Portal (<https://portal.gdc.cancer.gov/>). The Notch pathway gene z-score of each participant was defined as the sum of z-scores of 32 genes of the “HALLMARK_NOTCH_SIGNALING” download from MSigDB (<https://www.gsea-msigdb.org/gsea/msigdb>). For each gene, $z\text{-score} = (x - \mu) / \sigma$; x is the normalized gene expression value, μ is the average of gene expression, and σ is the standard deviation of gene expression.

RT-qPCR

Purified RNA was reverse transcribed using SuperScript III First-Strand Synthesis (Thermo Fisher Scientific; 11752050). qPCRs were performed with PowerUp SYBR Green (Applied Biosystems; A25742) and primers listed in Table S6 using the ViiA7 Real-Time PCR System (Applied Biosystems).

PCR analysis

DNA was purified from isolated glands using TRIzol following the manufacturer’s protocol. PCRs were performed using a fluorescein amidite-labeled forward primer according to a published protocol (Bacher et al., 2005). Amplicon sizes were obtained using Peak Scanner.

scRNA-seq

The stomach glands of an *Atp4b*^{Cre};*Rosa26*^{NICD};*Arid1a*^{flox/flox} mouse at 23 wk were isolated. Isolated glands were digested into a single-cell suspension using collagenase and dispase and stained using EPCAM (Ab95641) and Sytox Blue (Thermo Fisher Scientific; S34857). EPCAM^{high} and Sytox^{low} cells were sorted using the Moflo Astrios and submitted for scRNA-seq using the 10x Genomics platform.

scRNA-seq analysis

Raw reads were processed using the 10x Genomics Cell Ranger pipeline to align these to the reference transcriptome (mm10) and to generate gene cell count matrices. Initial quality control and clustering were performed with R package Seurat, version 2.3.0. To remove falsely identified cells, cells having a unique molecular identifier count <1,000 or genes that expressed <10% of cells were excluded from further analysis. For imputing missing expression values, we used the MAGIC (Markov affinity-based graph imputation of cells) program with optimal diffusion constant $t = 2$. Data normalization and scaling to remove unwanted sources of variation in principal component analysis were conducted using genes with highly variable expression. Identified clusters were represented using a t-distributed stochastic neighbor embedding plot. Differential gene expression analysis was then used to identify significantly differentially expressed genes within each cluster using the t test for significance.

Organoid treatment

The stomach glands were isolated and seeded in Matrigel Matrix GFR PhenolRF Mouse (Corning; 356231) in a 96-well plate. The organoids were cultured in a 1:4 dilution of conditioned media obtained from L-WRN cells (ATCC CRL-3276) according to a provided protocol (Miyoshi and Stappenbeck, 2013). To avoid selection of specific cell types from subculturing, organoids were analyzed at the indicated time point from the initial seeding of gastric glands without any passages. Viability was assayed using 3-(4,5-dimethylthiazol-2-yl)-2,5-diphenyltetrazolium bromide according to protocol, and the absorbance at 570 nm and 630 nm was read using a SpectraMax 340PC Microplate Reader (Hansen et al., 1989). The percentage viability was calculated by first subtracting the absorbance A570 nm–A630 nm value of each well by the A570 nm–A630 nm value of the negative control (only Matrigel), then divided by the value obtained for the DMSO-only control obtained in the same way. Combinatorial treatments of small molecules were performed in a minimum of three independent replicates at a low concentration of 0.05% DMSO to limit the effect of DMSO on organoid growth. To extract RNA, organoids were extracted from Matrigel using Cell Recovery Solution (Corning; 354253), and RNA was purified with the RNeasy Mini Kit (Qiagen; 74104) according to protocol.

Data availability

The scRNA-seq, RNA-seq, and ChIP-seq data used to support this study have been deposited in the Gene Expression Omnibus database (accession no. GSE144388).

Online supplemental material

Fig. S1 shows analysis of human GC data and characterizes *Arid1a* intact and *Arid1a* heterozygous tumors in vivo. Fig. S2 reports motif enrichment, apoptosis, mismatch repair, and microsatellite instability in *Arid1a* intact and *Arid1a* heterozygous tumors. Fig. S3 shows ARID1A expression in normal stomachs and characterizes parietal and MIST1⁺ cell-specific deletions of *Arid1a*. Fig. S4 shows analysis of p53 pathway and apoptosis in *Arid1a* homozygous tumors. Fig. S5 characterizes double deletion of *Arid1a*

and *Trp53* in gastric tumors. Table S1 shows the criteria used for histological scoring of mouse tumors. Table S2 provides information on enhancers in *Arid1a* intact and *Arid1a* heterozygous tumors. Table S3 shows expression of group A, group B, group C, and group D genes. Table S4 lists the markers of each cluster identified in the scRNA-seq of *Arid1a* homozygous tumors. Table S5 provides information on enhancers in *Arid1a* heterozygous and *Arid1a* homozygous tumors. Table S6 lists the primers used for RT-qPCR.

Acknowledgments

We thank Dr. Sean Egan for helpful discussion and Dr. David Alpers for the gift of gastric intrinsic factor antibody.

The work was supported by SickKids Foundation start-up funding, the Canadian Institutes of Health Research PJT-173266 grant, a Cancer Research Society grant, a SickKids Garron Family Cancer Centre Pitblado Basic/Translational Discovery grant, and a Concern Foundation award (T.H. Kim); the SickKids Restramp and Canada graduate and Ontario graduate scholarships (A.K.H. Loe); Canadian Institutes of Health Research and University of Toronto Medicine by Design postdoctoral fellowships (J.-E. Kim); the Taishan Scholar Program of Shandong Province (tsqn201812136) and the National Key Research and Development Project of China (2019YFA0111400; H. Guo); and a Natural Sciences and Engineering Research Council of Canada discovery grant (498706), the Canadian Institutes of Health Research New Investigator Award, and the Ontario Ministry of Research, Innovation and Science Early Researcher Award (H.H. He).

Author contributions: A.K.H. Loe designed and performed experiments, analyzed data, and wrote the manuscript; R. Francis initiated the project, performed RNA-seq and ChIP-seq experiments, and revised the manuscript; J. Seo analyzed single-cell data; L. Du and Y. Wang analyzed human GC samples; Ji-Eun Kim performed scRNA-seq; S.W. Hakim analyzed the histology of tumors; Jung-Eun Kim helped with in vitro culture studies; H.H. He supervised RNA-seq and ChIP-seq data analyses; H. Guo performed and supervised RNA-seq and ChIP-seq data analyses; and T.-H. Kim conceived and supervised the study, analyzed data, and revised the manuscript.

Disclosures: The authors declare no competing interests exist.

Submitted: 7 February 2020

Revised: 20 January 2021

Accepted: 5 March 2021

References

Aso, T., H. Uozaki, S. Morita, A. Kumagai, and M. Watanabe. 2015. Loss of ARID1A, ARID1B, and ARID2 expression during progression of gastric cancer. *Anticancer Res.* 35:6819–6827.

Bacher, J.W., W.M. Abdel Megid, M.G. Kent-First, and R.B. Halberg. 2005. Use of mononucleotide repeat markers for detection of microsatellite instability in mouse tumors. *Mol. Carcinog.* 44:285–292. <https://doi.org/10.1002/mc.20146>

Bitler, B.G., S. Wu, P.H. Park, Y. Hai, K.M. Aird, Y. Wang, Y. Zhai, A.V. Kossenkov, A. Vara-Ailor, F.J. Rauscher III, et al. 2017. ARID1A-mutated

ovarian cancers depend on HDAC6 activity. *Nat. Cell Biol.* 19:962–973. <https://doi.org/10.1038/ncb3582>

Cerami, E., J. Gao, U. Dogrusoz, B.E. Gross, S.O. Sumer, B.A. Aksoy, A. Jacobsen, C.J. Byrne, M.L. Heuer, E. Larsson, et al. 2012. The cBio cancer genomics portal: an open platform for exploring multidimensional cancer genomics data. *Cancer Discov.* 2:401–404. <https://doi.org/10.1158/2159-8290.CD-12-0095>

Correa, P., and M.B. Piazuelo. 2012. The gastric precancerous cascade. *J. Dig. Dis.* 13:2–9. <https://doi.org/10.1111/j.1751-2980.2011.00550.x>

Dobin, A., C.A. Davis, F. Schlesinger, J. Drenkow, C. Zaleski, S. Jha, P. Batut, M. Chaisson, and T.R. Gingeras. 2013. STAR: ultrafast universal RNA-seq aligner. *Bioinformatics.* 29:15–21. <https://doi.org/10.1093/bioinformatics/bts635>

Ferlay, J., M. Colombet, I. Soerjomataram, C. Mathers, D.M. Parkin, M. Piñeros, A. Znaor, and F. Bray. 2019. Estimating the global cancer incidence and mortality in 2018: GLOBOCAN sources and methods. *Int. J. Cancer.* 144:1941–1953. <https://doi.org/10.1002/ijc.31937>

Gao, J., B.A. Aksoy, U. Dogrusoz, G. Dresdner, B. Gross, S.O. Sumer, Y. Sun, A. Jacobsen, R. Sinha, E. Larsson, et al. 2013. Integrative analysis of complex cancer genomics and clinical profiles using the cBioPortal. *Sci. Signal.* 6:pl1. <https://doi.org/10.1126/scisignal.2004088>

Gao, X., P. Tate, P. Hu, R. Tjian, W.C. Skarnes, and Z. Wang. 2008. ES cell pluripotency and germ-layer formation require the SWI/SNF chromatin remodeling component BAF250a. *Proc. Natl. Acad. Sci. USA.* 105:6656–6661. <https://doi.org/10.1073/pnas.0801802105>

Gavin, D.P., H. Kusumo, H. Zhang, A. Guidotti, and S.C. Pandey. 2016. Role of growth arrest and DNA damage-inducible, beta in alcohol-drinking behaviors. *Alcohol. Clin. Exp. Res.* 40:263–272. <https://doi.org/10.1111/acer.12965>

Guan, B., T.L. Wang, and I.-M. Shih. 2011. ARID1A, a factor that promotes formation of SWI/SNF-mediated chromatin remodeling, is a tumor suppressor in gynecologic cancers. *Cancer Res.* 71:6718–6727. <https://doi.org/10.1158/0008-5472.CAN-11-1562>

Han, N., M.A. Kim, H.S. Lee, and W.H. Kim. 2016. Loss of ARID1A expression is related to gastric cancer progression, Epstein-Barr virus infection, and mismatch repair deficiency. *Appl. Immunohistochem. Mol. Morphol.* 24:320–325. <https://doi.org/10.1097/PAI.0000000000000199>

Hansen, M.B., S.E. Nielsen, and K. Berg. 1989. Re-examination and further development of a precise and rapid dye method for measuring cell growth/cell kill. *J. Immunol. Methods.* 119:203–210. [https://doi.org/10.1016/0022-1759\(89\)90397-9](https://doi.org/10.1016/0022-1759(89)90397-9)

Hayakawa, Y., H. Ariyama, J. Stancikova, K. Sakitani, S. Asfaha, B.W. Renz, Z.A. Dubeykovskaya, W. Shibata, H. Wang, C.B. Westphalen, et al. 2015. Mist1 expressing gastric stem cells maintain the normal and neoplastic gastric epithelium and are supported by a perivascular stem cell niche. *Cancer Cell.* 28:800–814. <https://doi.org/10.1016/j.ccell.2015.10.003>

Hiramatsu, Y., A. Fukuda, S. Ogawa, N. Goto, K. Ikuta, M. Tsuda, Y. Matsumoto, Y. Kimura, T. Yoshioka, Y. Takada, et al. 2019. Arid1a is essential for intestinal stem cells through Sox9 regulation. *Proc. Natl. Acad. Sci. USA.* 116:1704–1713. <https://doi.org/10.1073/pnas.1804858116>

Huang, K.K., K. Ramnarayanan, F. Zhu, S. Srivastava, C. Xu, A.L.K. Tan, M. Lee, S. Tay, K. Das, M. Xing, et al. 2018. Genomic and epigenomic profiling of high-risk intestinal metaplasia reveals molecular determinants of progression to gastric cancer. *Cancer Cell.* 33:137–150.e5. <https://doi.org/10.1016/j.ccell.2017.11.018>

Inada, R., S. Sekine, H. Taniguchi, H. Tsuda, H. Katai, T. Fujiwara, and R. Kushima. 2015. ARID1A expression in gastric adenocarcinoma: clinicopathological significance and correlation with DNA mismatch repair status. *World J. Gastroenterol.* 21:2159–2168. <https://doi.org/10.3748/wjg.v21.i7.2159>

Kadoch, C., and G.R. Crabtree. 2015. Mammalian SWI/SNF chromatin remodeling complexes and cancer: mechanistic insights gained from human genomics. *Sci. Adv.* 1:e1500447. <https://doi.org/10.1126/sciadv.1500447>

Kang, D.H., D.J. Lee, S. Lee, S.Y. Lee, Y. Jun, Y. Kim, Y. Kim, J.S. Lee, D.K. Lee, S. Lee, et al. 2017. Interaction of tankyrase and peroxiredoxin II is indispensable for the survival of colorectal cancer cells. *Nat. Commun.* 8:40. <https://doi.org/10.1038/s41467-017-00054-0>

Kim, T.H., and R.A. Shivdasani. 2011. Notch signaling in stomach epithelial stem cell homeostasis. *J. Exp. Med.* 208:677–688. <https://doi.org/10.1084/jem.20101737>

Kimura, Y., A. Fukuda, S. Ogawa, T. Maruno, Y. Takada, M. Tsuda, Y. Hiramatsu, O. Araki, M. Nagao, T. Yoshikawa, et al. 2018. ARID1A maintains differentiation of pancreatic ductal cells and inhibits development of pancreatic ductal adenocarcinoma in mice. *Gastroenterology.* 155:194–209.e2. <https://doi.org/10.1053/j.gastro.2018.03.039>

- Koh, D.I., D. Han, H. Ryu, W.I. Choi, B.N. Jeon, M.K. Kim, Y. Kim, J.Y. Kim, L. Parry, A.R. Clarke, et al. 2014. KAISO, a critical regulator of p53-mediated transcription of CDKN1A and apoptotic genes. *Proc. Natl. Acad. Sci. USA*. 111:15078–15083. <https://doi.org/10.1073/pnas.1318780111>
- Langmead, B., and S.L. Salzberg. 2012. Fast gapped-read alignment with Bowtie 2. *Nat. Methods*. 9:357–359. <https://doi.org/10.1038/nmeth.1923>
- Li, G.M. 2008. Mechanisms and functions of DNA mismatch repair. *Cell Res*. 18:85–98. <https://doi.org/10.1038/cr.2007.115>
- Manabe, Y., M. Tohigi, A. Moriwaki, S. Takeuchi, and S. Takahashi. 2013. Insulin-like growth factor 1 mRNA expression in the uterus of streptozotocin-treated diabetic mice. *J. Reprod. Dev.* 59:398–404. <https://doi.org/10.1262/jrd.2012-169>
- Marino, S., M. Vooijs, H. van Der Gulden, J. Jonkers, and A. Berns. 2000. Induction of medulloblastomas in p53-null mutant mice by somatic inactivation of Rb in the external granular layer cells of the cerebellum. *Genes Dev*. 14:994–1004.
- Matheu, A., A. Maraver, P. Klatt, I. Flores, I. Garcia-Cao, C. Borrás, J.M. Flores, J. Viña, M.A. Blasco, and M. Serrano. 2007. Delayed ageing through damage protection by the Arf/p53 pathway. *Nature*. 448:375–379. <https://doi.org/10.1038/nature05949>
- Mathur, R., B.H. Alver, A.K. San Roman, B.G. Wilson, X. Wang, A.T. Agoston, P.J. Park, R.A. Shivdasani, and C.W. Roberts. 2017. ARID1A loss impairs enhancer-mediated gene regulation and drives colon cancer in mice. *Nat. Genet.* 49:296–302. <https://doi.org/10.1038/ng.3744>
- Miyoshi, H., and T.S. Stappenbeck. 2013. In vitro expansion and genetic modification of gastrointestinal stem cells in spheroid culture. *Nat. Protoc.* 8:2471–2482. <https://doi.org/10.1038/nprot.2013.153>
- Murtaugh, L.C., B.Z. Stanger, K.M. Kwan, and D.A. Melton. 2003. Notch signaling controls multiple steps of pancreatic differentiation. *Proc. Natl. Acad. Sci. USA*. 100:14920–14925. <https://doi.org/10.1073/pnas.2436557100>
- Nagl, N.G. Jr., A. Patsialou, D.S. Haines, P.B. Dallas, G.R. Beck Jr., and E. Moran. 2005. The p270 (ARID1A/SMARCF1) subunit of mammalian SWI/SNF-related complexes is essential for normal cell cycle arrest. *Cancer Res*. 65:9236–9244. <https://doi.org/10.1158/0008-5472.CAN-05-1225>
- Nakayama, K., M.M. Szweczyk, C. Dela Sena, H. Wu, A. Dong, H. Zeng, F. Li, R.F. de Freitas, M.S. Eram, M. Schapira, et al. 2018. TP-064, a potent and selective small molecule inhibitor of PRMT4 for multiple myeloma. *Oncotarget*. 9:18480–18493. <https://doi.org/10.18632/oncotarget.24883>
- Petersen, C.P., J.C. Mills, and J.R. Goldenring. 2017. Murine models of gastric corpus preneoplasia. *Cell. Mol. Gastroenterol. Hepatol.* 3:11–26. <https://doi.org/10.1016/j.jcmgh.2016.11.001>
- Pruunsild, P., C.P. Bengtson, and H. Bading. 2017. Networks of cultured iPSC-derived neurons reveal the human synaptic activity-regulated adaptive gene program. *Cell Rep*. 18:122–135. <https://doi.org/10.1016/j.celrep.2016.12.018>
- Robinson, J.T., H. Thorvaldsdóttir, W. Winckler, M. Guttman, E.S. Lander, G. Getz, and J.P. Mesirov. 2011. Integrative Genomics Viewer. *Nat. Biotechnol.* 29:24–26. <https://doi.org/10.1038/nbt.1754>
- Stange, D.E., B.K. Koo, M. Huch, G. Sibbel, O. Basak, A. Lyubimova, P. Kujala, S. Bartfeld, J. Koster, J.H. Geahlen, et al. 2013. Differentiated Troy⁺ chief cells act as reserve stem cells to generate all lineages of the stomach epithelium. *Cell*. 155:357–368. <https://doi.org/10.1016/j.cell.2013.09.008>
- Sun, X., S.C. Wang, Y. Wei, X. Luo, Y. Jia, L. Li, P. Gopal, M. Zhu, I. Nassour, J.C. Chuang, et al. 2017. Arid1a has context-dependent oncogenic and tumor suppressor functions in liver cancer. *Cancer Cell*. 32:574–589.e6. <https://doi.org/10.1016/j.ccell.2017.10.007>
- Syder, A.J., S.M. Karam, J.C. Mills, J.E. Ippolito, H.R. Ansari, V. Farook, and J.I. Gordon. 2004. A transgenic mouse model of metastatic carcinoma involving transdifferentiation of a gastric epithelial lineage progenitor to a neuroendocrine phenotype. *Proc. Natl. Acad. Sci. USA*. 101:4471–4476. <https://doi.org/10.1073/pnas.0307983101>
- Takaishi, S., T. Okumura, S. Tu, S.S. Wang, W. Shibata, R. Vigneshwaran, S.A. Gordon, Y. Shimada, and T.C. Wang. 2009. Identification of gastric cancer stem cells using the cell surface marker CD44. *Stem Cells*. 27:1006–1020. <https://doi.org/10.1002/stem.30>
- Tang, Z., P. Arjunan, C. Lee, Y. Li, A. Kumar, X. Hou, B. Wang, P. Wardega, F. Zhang, L. Dong, et al. 2010. Survival effect of PDGF-CC rescues neurons from apoptosis in both brain and retina by regulating GSK3beta phosphorylation. *J. Exp. Med.* 207:867–880. <https://doi.org/10.1084/jem.20091704>
- The Cancer Genome Atlas Research Network. 2014. Comprehensive molecular characterization of gastric adenocarcinoma. *Nature*. 513:202–209. <https://doi.org/10.1038/nature13480>
- Vassilev, L.T., B.T. Vu, B. Graves, D. Carvajal, F. Podlaski, Z. Filipovic, N. Kong, U. Kammlott, C. Lukacs, C. Klein, et al. 2004. In vivo activation of the p53 pathway by small-molecule antagonists of MDM2. *Science*. 303:844–848. <https://doi.org/10.1126/science.1092472>
- Wang, K., J. Kan, S.T. Yuen, S.T. Shi, K.M. Chu, S. Law, T.L. Chan, Z. Kan, A.S. Chan, W.Y. Tsui, et al. 2011. Exome sequencing identifies frequent mutation of ARID1A in molecular subtypes of gastric cancer. *Nat. Genet.* 43:1219–1223. <https://doi.org/10.1038/ng.982>
- Wang, L., Z. Zhao, M.B. Meyer, S. Saha, M. Yu, A. Guo, K.B. Wisinski, W. Huang, W. Cai, J.W. Pike, et al. 2014. CARM1 methylates chromatin remodeling factor BAF155 to enhance tumor progression and metastasis. *Cancer Cell*. 25:21–36. <https://doi.org/10.1016/j.ccr.2013.12.007>
- Wang, S.C., I. Nassour, S. Xiao, S. Zhang, X. Luo, J. Lee, L. Li, X. Sun, L.H. Nguyen, J.C. Chuang, et al. 2019. SWI/SNF component ARID1A restrains pancreatic neoplasia formation. *Gut*. 68:1259–1270. <https://doi.org/10.1136/gutjnl-2017-315490>
- Watanabe, T., G. Tanaka, S. Hamada, C. Namiki, T. Suzuki, M. Nakajima, and C. Furihata. 2009. Dose-dependent alterations in gene expression in mouse liver induced by diethylnitrosamine and ethylnitrosourea and determined by quantitative real-time PCR. *Mutat. Res.* 673:9–20. <https://doi.org/10.1016/j.mrgentox.2008.11.004>
- Wu, J.N., and C.W. Roberts. 2013. ARID1A mutations in cancer: another epigenetic tumor suppressor? *Cancer Discov.* 3:35–43. <https://doi.org/10.1158/2159-8290.CD-12-0361>
- Wu, R.C., T.L. Wang, and I.-M. Shih. 2014. The emerging roles of ARID1A in tumor suppression. *Cancer Biol. Ther.* 15:655–664. <https://doi.org/10.4161/cbt.28411>
- Yadava, R.S., E.P. Foff, Q. Yu, J.T. Gladman, T.S. Zheng, and M.S. Mahadevan. 2016. TWEAK regulates muscle functions in a mouse model of RNA toxicity. *PLoS One*. 11:e0150192. <https://doi.org/10.1371/journal.pone.0150192>
- Yan, H.B., X.F. Wang, Q. Zhang, Z.Q. Tang, Y.H. Jiang, H.Z. Fan, Y.H. Sun, P.Y. Yang, and F. Liu. 2014. Reduced expression of the chromatin remodeling gene ARID1A enhances gastric cancer cell migration and invasion via downregulation of E-cadherin transcription. *Carcinogenesis*. 35:867–876. <https://doi.org/10.1093/carcin/bgt398>
- Yang, F., Y. Xu, C. Liu, C. Ma, S. Zou, X. Xu, J. Jia, and Z. Liu. 2018. NF-κB/miR-223-3p/ARID1A axis is involved in *Helicobacter pylori* CagA-induced gastric carcinogenesis and progression. *Cell Death Dis.* 9:12. <https://doi.org/10.1038/s41419-017-0020-9>
- Yang, L., S. Wei, R. Zhao, Y. Wu, H. Qiu, and H. Xiong. 2016. Loss of ARID1A expression predicts poor survival prognosis in gastric cancer: a systematic meta-analysis from 14 studies. *Sci. Rep.* 6:28919. <https://doi.org/10.1038/srep28919>
- Yao, Y., Y. Ni, J. Zhang, H. Wang, and S. Shao. 2017. The role of Notch signaling in gastric carcinoma: molecular pathogenesis and novel therapeutic targets. *Oncotarget*. 8:53839–53853. <https://doi.org/10.18632/oncotarget.17809>
- Yu, G., L.G. Wang, Y. Han, and Q.Y. He. 2012. clusterProfiler: an R package for comparing biological themes among gene clusters. *OMICS*. 16:284–287. <https://doi.org/10.1089/omi.2011.0118>
- Yu, G., L.G. Wang, and Q.Y. He. 2015. ChIPseeker: an R/Bioconductor package for ChIP peak annotation, comparison and visualization. *Bioinformatics*. 31:2382–2383. <https://doi.org/10.1093/bioinformatics/btv145>
- Zang, Z.J., I. Cutcutache, S.L. Poon, S.L. Zhang, J.R. McPherson, J. Tao, V. Rajasegaran, H.L. Heng, N. Deng, A. Gan, et al. 2012. Exome sequencing of gastric adenocarcinoma identifies recurrent somatic mutations in cell adhesion and chromatin remodeling genes. *Nat. Genet.* 44:570–574. <https://doi.org/10.1038/ng.2246>
- Zhai, Y., R. Kuick, C. Tipton, R. Wu, M. Sessine, Z. Wang, S.J. Baker, E.R. Fearon, and K.R. Cho. 2016. Arid1a inactivation in an Apc- and Pten-defective mouse ovarian cancer model enhances epithelial differentiation and prolongs survival. *J. Pathol.* 238:21–30. <https://doi.org/10.1002/path.4599>
- Zhang, K., and R.J. Kaufman. 2008. Identification and characterization of endoplasmic reticulum stress-induced apoptosis in vivo. *Methods Enzymol.* 442:395–419. [https://doi.org/10.1016/S0076-6879\(08\)01420-1](https://doi.org/10.1016/S0076-6879(08)01420-1)
- Zhang, Y., T. Liu, C.A. Meyer, J. Eeckhoutte, D.S. Johnson, B.E. Bernstein, C. Nusbaum, R.M. Myers, M. Brown, W. Li, et al. 2008. Model-based analysis of ChIP-Seq (MACS). *Genome Biol.* 9:R137. <https://doi.org/10.1186/gb-2008-9-9-r137>

Supplemental material

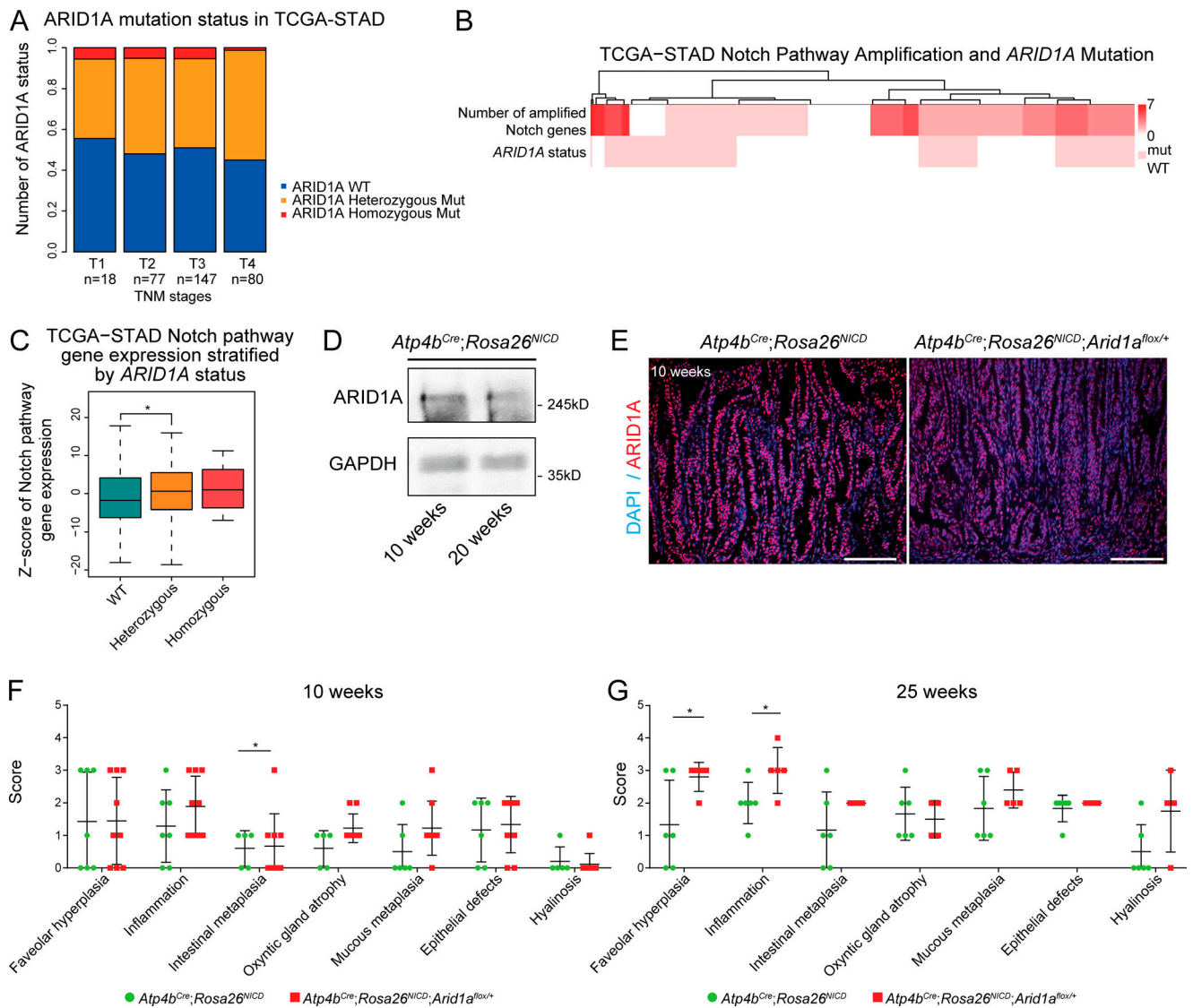


Figure S1. **ARID1A heterozygous loss promotes tumor progression in Notch-activated gastric adenoma.** (A) Analysis of *ARID1A* alterations in different human GC stages based on data obtained from TCGA (STAD, Firehose) identifies an increased proportion of *ARID1A* heterozygous alterations in the more advanced stages. TNM, tumor, node, metastasis. (B) Analysis of TCGA-STAD data showing the overlap of human GC cases with amplifications in Notch pathway genes and *ARID1A* mutations. The top row of the heatmap indicates the number of Notch pathway genes amplified, and the bottom row indicates the samples with or without *ARID1A* mutation. (C) Analysis of Notch pathway gene expression in human gastric cancer cases with *ARID1A* alterations from TCGA-STAD data shows significantly increased Notch pathway gene expression in *ARID1A* heterozygous cancer cases compared with *ARID1A* wild-type cancer cases (*, $P < 0.04491$, unpaired t test). (D) Western blot of *ARID1A* from the tumor epithelial cells of 10- and 20-wk-old Notch-activated adenoma mice. (E) Representative immunofluorescence images of *ARID1A* staining in *Arid1a* intact and *Arid1a* heterozygous gastric tumors demonstrate that *ARID1A* expression is not completely lost in *Arid1a* heterozygous tumors ($n = 3$ each). Scale bar, 100 μm . (F) Individual disease scores of 10-wk-old *Arid1a* intact and *Arid1a* heterozygous gastric tumors using Table S1 (*, $P < 0.05$; unpaired t test). Bars represent mean \pm SD. (G) Individual disease scores of *Arid1a* intact and *Arid1a* heterozygous gastric tumors at 25 wk of age using Table S1 (*, $P < 0.05$; unpaired t test). Bars represent mean \pm SD.

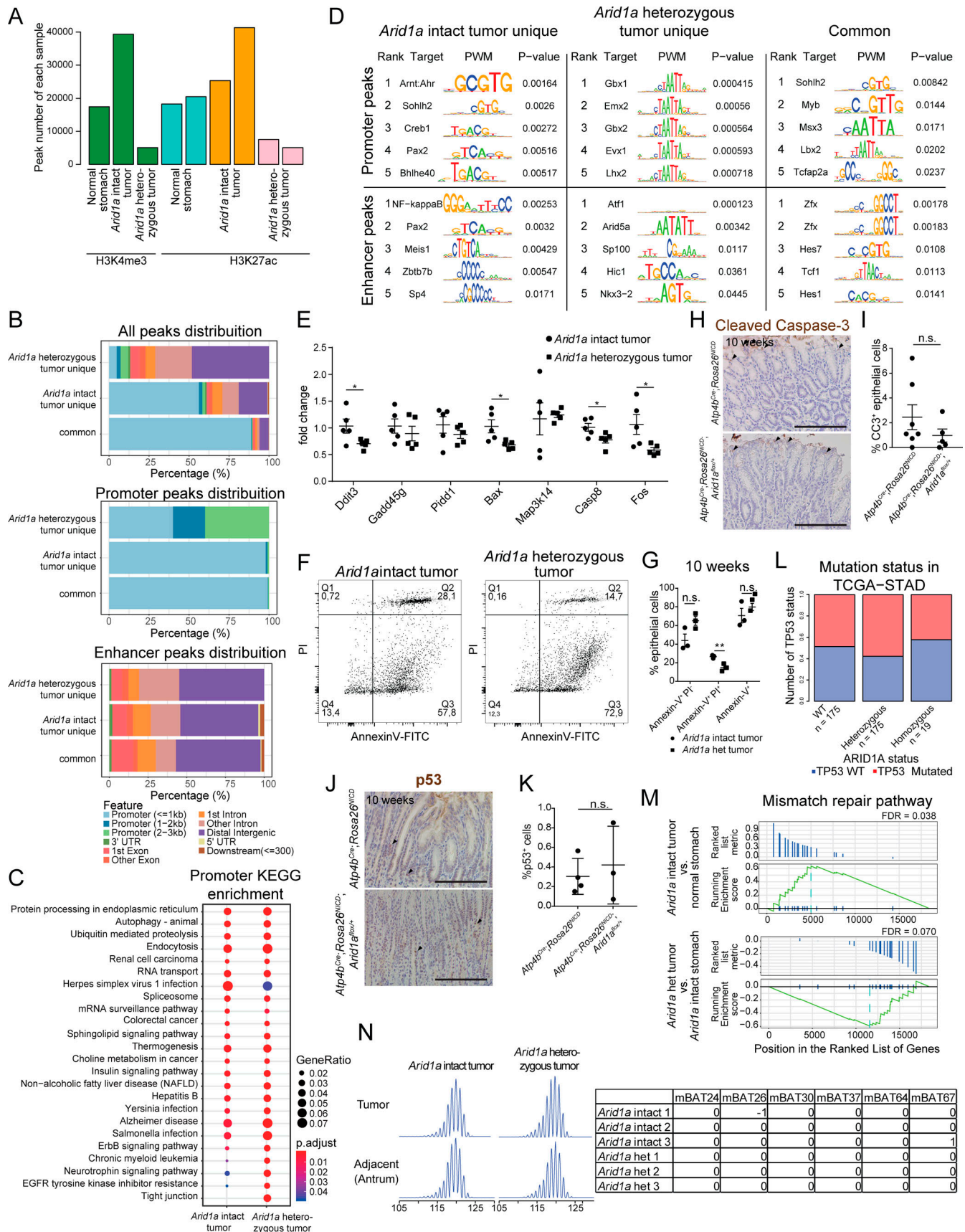


Figure S2. **Chromatin and transcriptomic analyses of *Arid1a* intact tumors and *Arid1a* heterozygous tumors.** **(A)** Number of H3K4me3 and H3K27ac peaks per biological replicate in the wild-type stomach and *Arid1a* intact and *Arid1a* heterozygous tumors. **(B)** Feature distribution of all H3K27ac peaks (top), promoter peaks (middle), and enhancer peaks (bottom) specific to either *Arid1a* intact tumors or *Arid1a* heterozygous tumors or shared between both. UTR, untranslated region. **(C)** Kyoto Encyclopedia of Genes and Genomes (KEGG) pathway enrichment analysis of promoter H3K27ac peaks that are specific to or shared between *Arid1a* intact and *Arid1a* heterozygous tumors. EGFR, epidermal growth factor receptor. **(D)** Motif enrichment analysis of H3K27 peaks of *Arid1a* intact and *Arid1a* heterozygous tumors. PWM, position weight matrix. **(E)** RT-qPCR of p53- and apoptosis-related genes in *Arid1a* intact and *Arid1a* heterozygous tumors. Bars represent mean \pm SEM. **(F)** FACS plots of annexin V and PI staining of epithelial cells isolated from *Arid1a* intact and *Arid1a* heterozygous tumors at 10 wk of age. **(G)** Quantification of annexin V⁺ and PI⁺ epithelial cells isolated from 10-wk-old *Arid1a* intact and *Arid1a* heterozygous tumors shows significant reduction of late-stage apoptotic cells (annexin V⁺ PI⁺) in *Arid1a* heterozygous tumors compared with *Arid1a* intact tumors ($P = 0.0096$, unpaired t test). Bars represent mean \pm SEM. **(H)** Representative images of cleaved caspase-3 staining in normal stomach and *Arid1a* heterozygous tumors. Arrowheads indicate cleaved caspase-3⁺ cells. ($n = 7$ and $n = 5$, respectively). Scale bar, 100 μ m. **(I)** Quantification of the number of cleaved caspase-3⁺ cells in the normal stomachs and *Arid1a* heterozygous tumors (unpaired t test). Bars represent mean \pm SEM. **(J)** Representative images of p53 staining in normal stomach and *Arid1a* heterozygous tumors. Arrowheads indicate p53⁺ cells. ($n = 4$ and $n = 3$, respectively). Scale bar, 100 μ m. **(K)** Quantification of the number of p53⁺ cells in the normal stomachs and *Arid1a* heterozygous tumors (unpaired t test). Bars represent mean \pm SEM. **(L)** Analysis of *TP53* mutation status in human gastric cancer cases with or without *ARID1A* alterations using TCGA-STAD data. **(M)** Gene set enrichment analysis of mismatch repair pathway using RNA-seq data of normal stomach, *Arid1a* intact tumors, and *Arid1a* heterozygous tumors. FDR, false discovery rate. **(N)** PCR analysis of mononucleotide repeat loci in the *Arid1a* intact and *Arid1a* heterozygous tumor mice. Left: An example of peak spectra indicating the size of the PCR product obtained from epithelial cells isolated from tumor and adjacent benign (antrum) regions. Right: Summary of the differences in PCR product size obtained from epithelial cells isolated from tumor and adjacent benign region using the corresponding primers (Bacher et al., 2005).

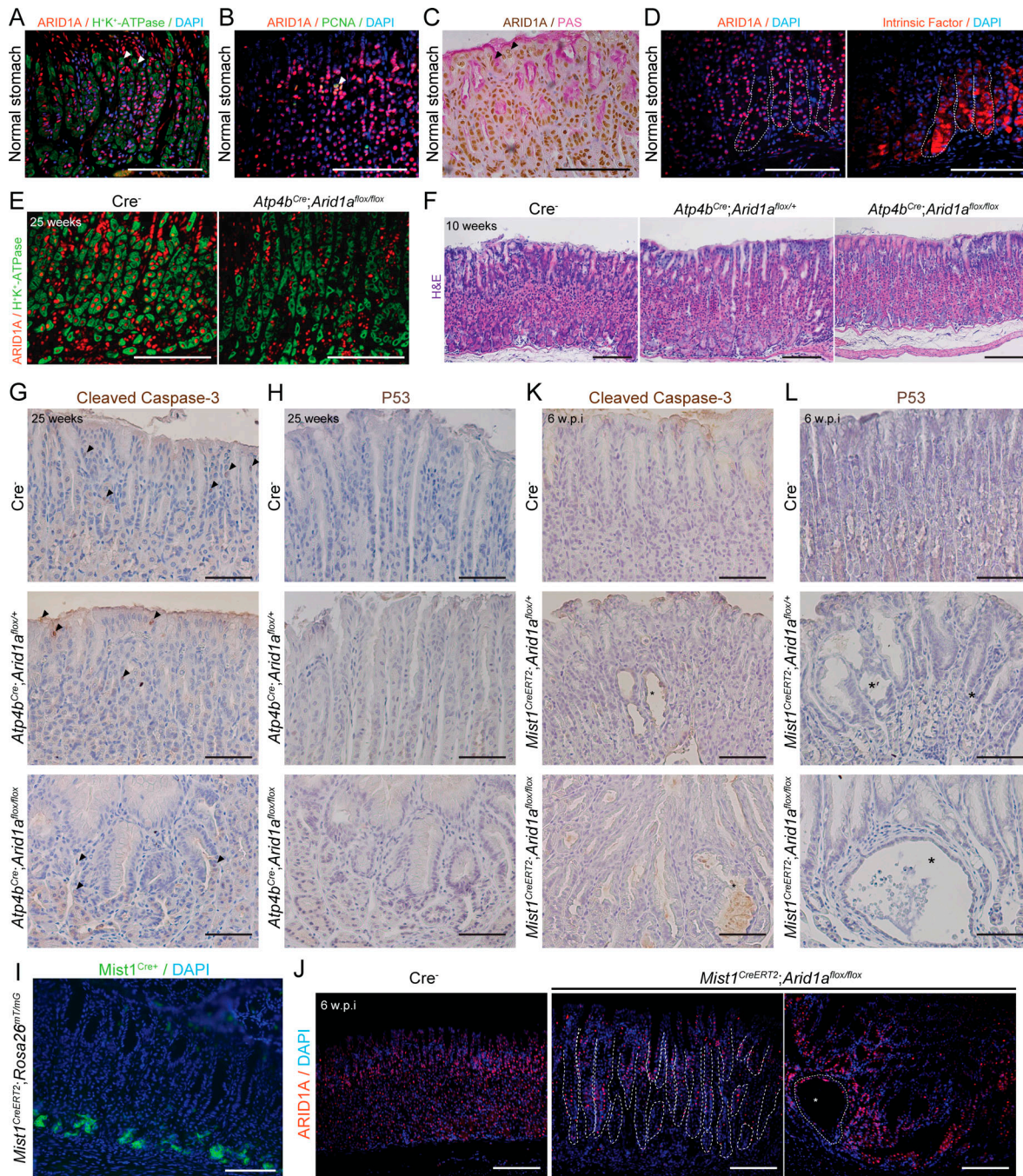


Figure S3. **Analysis of cell type-specific ARID1A loss during adult gastric homeostasis.** (A) Costaining of ARID1A and parietal cell marker, H⁺-K⁺-ATPase. Arrowheads indicate examples of H⁺-K⁺-ATPase and ARID1A double positive cells. Scale bar, 100 μ m. (B) Costaining of ARID1A and proliferating cell marker PCNA. Arrowheads indicate examples of PCNA and ARID1A double positive cells. Scale bar, 100 μ m. (C) Costaining of ARID1A with PAS staining, which labels gastric pit cells. Arrowheads indicate examples of PAS and ARID1A double positive cells. Scale bar, 100 μ m. (D) Staining of ARID1A and chief cell marker, intrinsic factor using serial histological sections. Scale bar, 100 μ m. (E) Representative immunofluorescence images of ARID1A and H⁺-K⁺-ATPase costaining in the murine stomachs of normal (wild-type) and parietal cell-specific deletion of *Arid1a*, displaying effective deletion of *Arid1a* in target cells ($n = 3$). Scale bar, 100 μ m. (F) Representative histological images of normal stomach and the stomach of mice with one or both copies *Arid1a* deleted in parietal cells ($n = 3$ each). Scale bar, 100 μ m. (G) Representative images of cleaved caspase-3 staining in normal stomach and the stomach of mice with one or both copies *Arid1a* deleted in parietal cells; arrowhead denotes cleaved caspase-3⁺ cells ($n = 3$ each). Scale bar, 100 μ m. (H) Representative images of p53 staining in normal stomach and the stomach of mice with one or both copies *Arid1a* deleted in parietal cells ($n = 3$ each). Scale bar, 100 μ m. (I) Expression of membrane GFP in the stomach of *Mist1^{CreERT2};Rosa26^{mT/mG}* mice 2 d after the last dose of tamoxifen injection. Scale bar, 100 μ m. (J) Staining of ARID1A in the stomach of *Mist1^{CreERT2};Arid1a^{fllox/fllox}* and injected *Cre⁻* control mice 6 w.p.i., showing effective deletion of ARID1A in a large region of the stomach epithelium. Dotted white lines outline individual glands, and asterisk indicates a cystic region in *Mist1^{CreERT2};Arid1a^{fllox/fllox}* mice ($n = 3$ each). Scale bar, 100 μ m. (K) Representative images of cleaved caspase-3 staining in the stomach of *Mist1^{CreERT2};Arid1a^{fllox/+}*, *Mist1^{CreERT2};Arid1a^{fllox/fllox}*, and injected control mice at 6 w.p.i. ($n = 3$ each). Scale bar, 100 μ m. (L) Representative images of p53 staining in the stomach of *Mist1^{CreERT2};Arid1a^{fllox/+}*, *Mist1^{CreERT2};Arid1a^{fllox/fllox}*, and injected control mice at 6 w.p.i. ($n = 3$ each). Scale bar, 100 μ m.

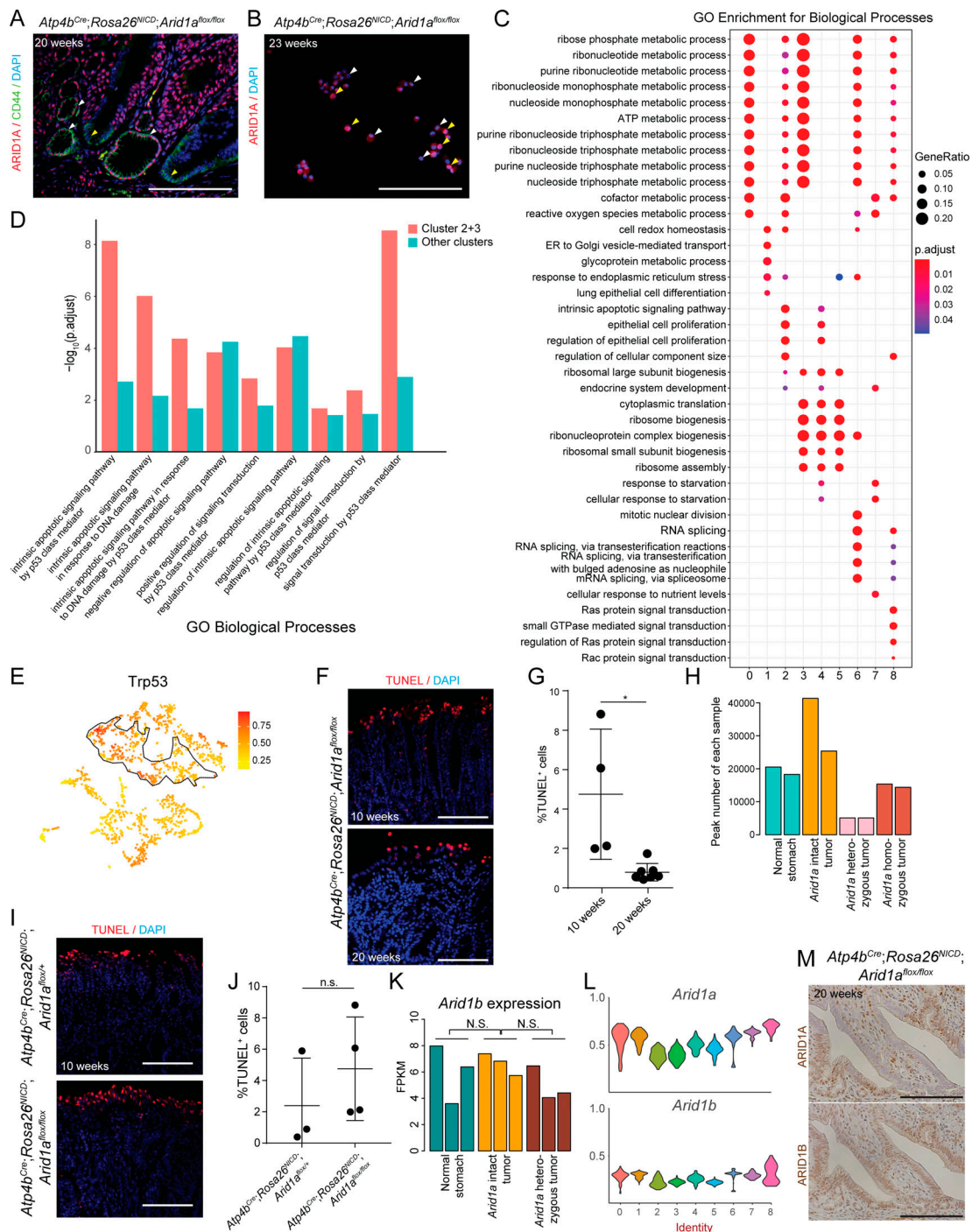


Figure S4. Single-cell analysis of *Arid1a* homozygous tumor. (A) Representative immunofluorescence image of ARID1A and CD44 costaining of *Arid1a* homozygous tumors at 20 wk shows both ARID1A⁺ CD44⁺ (white arrowhead) and ARID1A⁻ CD44⁺ (yellow arrowhead) cells ($n = 3$). Scale bar, 100 μm . (B) Immunofluorescence image of ARID1A staining of epithelial cells isolated from *Arid1a* homozygous tumors in preparation for scRNA-seq; the white arrowhead denotes the ARID1A⁻ cells, and yellow arrowheads denote the ARID1A⁺ cells ($n = 3$). Scale bar, 100 μm . (C) GO term analysis of clustering markers of epithelial cells in *Arid1a* homozygous tumors. (D) Analysis of GO terms related to p53 signaling and apoptosis displays increased enrichment in clusters 2 and 3 compared with the other clusters. (E) Feature plots of the scRNA-seq data shows enriched expression of *Trp53* in clusters 2 and 3 (dotted line). (F) Representative images of TUNEL staining in *Arid1a* homozygous gastric tumors at 10 and 20 wk ($n = 4$ and 7, respectively). Scale bar, 100 μm . (G) Quantification of TUNEL⁺ cells in *Arid1a* homozygous gastric tumors at 10 and 20 wk (*, $P = 0.01$, unpaired t test). Bars represent mean \pm SD. (H) Number of H3K27ac peaks per replicate in normal *Cre*⁻ stomach, *Arid1a* intact, *Arid1a* heterozygous, and *Arid1a* homozygous tumors. (I) Representative images of TUNEL fluorescence staining in *Arid1a* heterozygous and homozygous gastric tumors at 10 wk ($n = 3$ and 4, respectively). Scale bar, 100 μm . (J) Quantification of TUNEL⁺ cells in *Arid1a* heterozygous and homozygous gastric tumors at 10 wk (unpaired t test). Bars represent mean \pm SD. (K) Expression of *Arid1b* in wild-type stomachs ($n = 3$), *Arid1a* intact tumors ($n = 3$), and *Arid1a* heterozygous tumors ($n = 3$) from RNA-seq (unpaired t test). (L) Violin plots of *Arid1a* and *Arid1b* expression from scRNA-seq of *Arid1a* homozygous tumors. (M) Representative images of ARID1A and ARID1B antibody staining in serial sections of 20-wk-old *Arid1a* homozygous tumors shows expression of ARID1B in both ARID1A⁻ and ARID1A⁺ regions ($n = 4$). Scale bars, 100 μm .

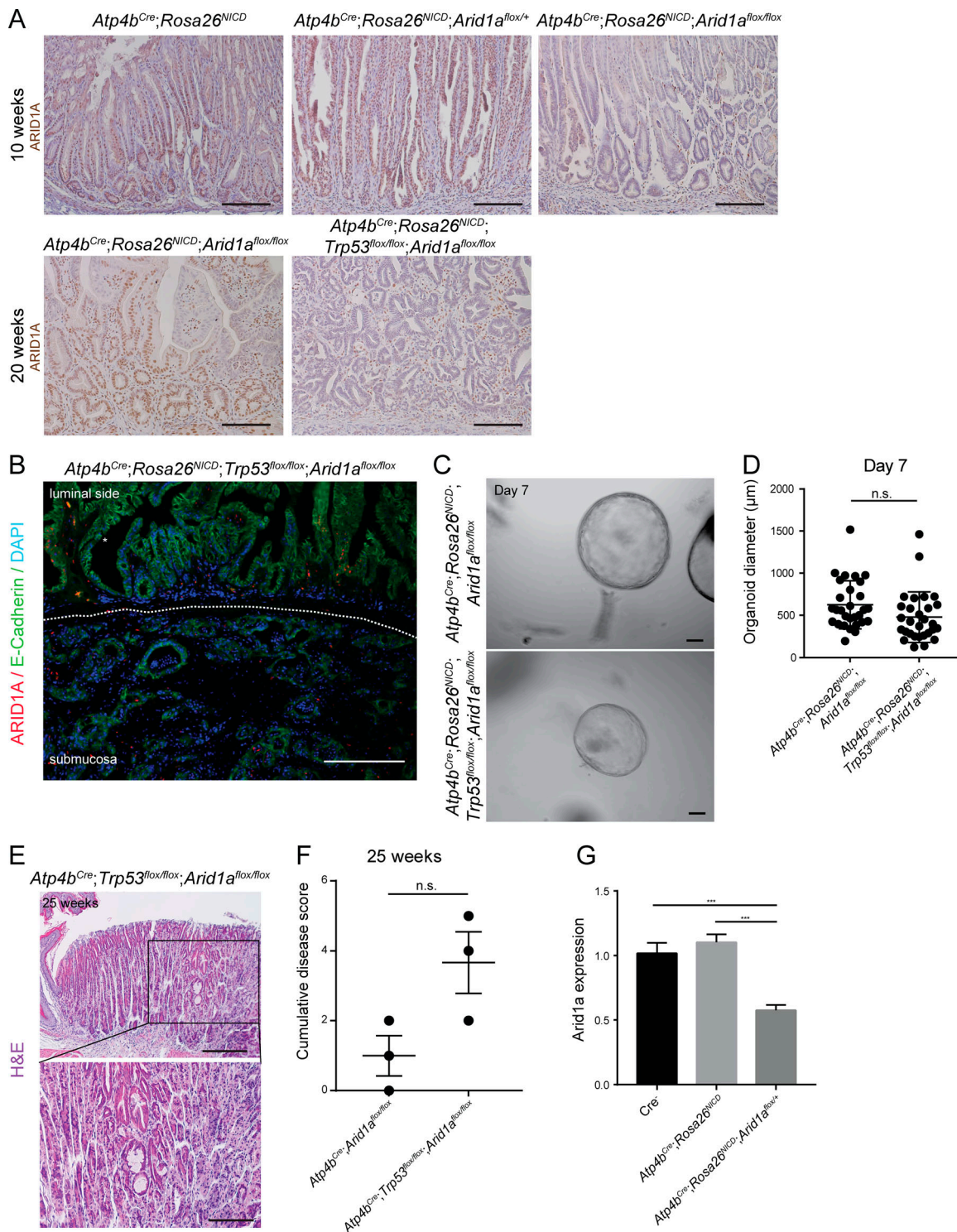


Figure S5. **Analysis of Trp53 deletion in *Arid1a* homozygous tumors.** (A) Representative images of ARID1A staining by histochemistry in 10-wk and 20-wk *Arid1a* intact, *Arid1a* heterozygous, and *Arid1a* homozygous tumors ($n = 3$ each). Scale bar, 100 μm . (B) Representative image of ARID1A and E-cadherin costaining in gastric tumor with double deletion of *Arid1a* and *Trp53* ($n = 3$). Scale bar, 100 μm . (C) Representative images of organoids established from the epithelial cells of *Arid1a* homozygous tumors or *Arid1a*;*Trp53* double-deletion tumors. Experiments were repeated twice with organoids obtained from two different mice for each genotype. Scale bars, 100 μm . (D) Quantification of the diameter of organoids established from the epithelial cells of *Arid1a* homozygous tumors and *Arid1a*;*Trp53* double-deletion tumors (unpaired t test). Bars represent mean \pm SD. (E) Representative histological images of stomach with double deletion of *Arid1a* and *Trp53* in gastric parietal cells at 25 wk ($n = 3$). Scale bar, 100 μm . (F) Histopathological scoring of stomachs with *Arid1a* deletion and *Arid1a*;*Trp53* double deletion in gastric parietal cells using features shown in Table S1 ($P = 0.065$, unpaired t test). Bars represent mean \pm SEM. (G) RT-qPCR analysis of *Arid1a* expression in normal stomachs and tumor organoids on day 4 of culture confirms down-regulation of *Arid1a* in *Arid1a* heterozygous tumor organoids. Experiments were repeated at least twice with organoids obtained from two different mice for each genotype (***, $P < 0.001$; unpaired t test). Error bars represent SEM.

Six tables are provided online. Table S1 shows the criteria used for histological scoring of mouse tumors. Table S2 provides information on enhancers in *Arid1a* intact and *Arid1a* heterozygous tumors. Table S3 shows expression of group A, group B, group C, and group D genes. Table S4 lists the markers of each cluster identified in the scRNA-seq of *Arid1a* homozygous tumors. Table S5 provides information on enhancers in *Arid1a* heterozygous and *Arid1a* homozygous tumors. Table S6 lists the primers used for RT-qPCR.